PHYSICAL REVIEW FLUIDS **1**, 083402 (2016)

Generalized Chapman-Enskog continuum breakdown parameters for chemically reacting flows

Krishnan Swaminathan-Gopalan, Sharanya Subramaniam, and Kelly A. Stephani[*]
Department of Mechanical Science and Engineering, University of Illinois at Urbana-Champaign, Urbana, Illinois 61801, USA

(Received 9 March 2016; published 9 December 2016)

The generalized Chapman-Enskog (GCE) method for rapid and slow thermochemical processes is employed to formulate a set of continuum breakdown parameters for chemically reacting flows. These GCE breakdown parameters are derived for one-temperature, two-temperature, and three-temperature models, through classification of the relevant thermochemical time scales relative to fast elastic collisional processes and slow flow processes associated with changes in macroscopic observables. Continuum breakdown mechanisms owing to multicomponent diffusion, thermal diffusion, normal and shear stresses, Fourier-type heat fluxes based on translational, rotational, and vibrational temperatures, bulk viscosity, and relaxation pressure are presented for chemically reacting flows. The GCE breakdown parameters, derived from rigorous kinetic theory, capture the proper physical mechanism leading to continuum breakdown. These breakdown parameters are used to analyze continuum breakdown in a Mach 24 reacting air flow over a sphere and continuum breakdown is observed in the shock and close to the sphere surface. The flow field near the sphere surface is found to be characterized by sharp species concentration gradients due to gas-phase and surface reactions. Chemical reactions thus lead indirectly to the distortion of the velocity distribution function (VDF), providing a pathway to continuum breakdown that is captured by the GCE specieswise diffusion breakdown parameter.

DOI: 10.1103/PhysRevFluids.1.083402

I. INTRODUCTION

Multiscale flows involving mixed regions of continuum and rarefied flow regimes are common in a variety of engineering applications, from microelectromechanical system devices to high-speed atmospheric entry vehicles. Simulation techniques developed for multiscale flow modeling require an accurate description of rarefaction effects, which are most suitably captured by kinetic solvers, such as direct methods for the Boltzmann equation or particle-based methods such as the direct simulation Monte Carlo (DSMC) method [1]. While kinetic methods may be employed from continuum to free molecular flow regimes, they are most commonly used for modeling nonequilibrium flows characterized by a Knudsen number $\mathrm{Kn} \geqslant 0.1$. Approaching the continuum limit, the flow field may be accurately modeled with continuum (Euler or Navier-Stokes) solvers, which provide a computationally efficient alternative to the kinetic solvers, but these solutions become inaccurate outside the hydrodynamic regime. It is precisely in this regime, however, that a high-fidelity kinetic solver may be employed. Thus, a combined continuum-kinetic approach is often adopted as a way to achieve high-fidelity solutions across a broad range of flow regimes, while maintaining computational efficiency.

Hybrid multiscale methods have been developed and successfully applied to a wide range of flow problems [2–6]. These combined approaches typically involve spatial coupling of computational fluid dynamics (CFD) solvers, based on Euler or Navier-Stokes continuum descriptions, with kinetic solvers, based on the Bhatnagar-Gross-Krook model, the direct Boltzmann method, or the particle-based DSMC method. One of the key components of hybrid solvers is defining the hybrid interface

---

[*] Corresponding author: ksteph@illinois.edu

as well as the interface location. The hybrid interface is a computational boundary in physical space dividing the regions of continuum and rarefied flow, facilitating the transfer of flow field information between the continuum and kinetic solvers. To maximize computational efficiency, it is important to determine where, in physical space, the continuum solution method begins to break down and the kinetic solution method should be employed.

The onset of continuum breakdown is characterized by a departure of the underlying velocity distribution function (VDF) from its equilibrium Maxwellian form. CFD solvers based on the Navier-Stokes equations provide accurate solutions for systems involving *small departures* from equilibrium, expressed mathematically as a perturbation of the Maxwellian distribution or the well-known Chapman-Enskog distribution [7]. Physically, the hydrodynamic quantities of number density, velocity, and temperature are carried by the equilibrium Maxwellian distribution, while the perturbation of the Maxwellian distribution manifests as higher-order fluxes, including heat flux as well as normal and shear stresses for a simple gas. The Navier-Stokes equations incorporate these higher-order effects in the governing equations through constitutive relationships, which provide closure for the equations and allow for the relation of internal stresses and heat fluxes to gradients of the macroscopic observables. Provided the departure from equilibrium is small, these constitutive relations hold and the Navier-Stokes equations are valid.

When flow field gradients become large or characteristic length scales become comparable to the molecular mean free path, the underlying VDF exhibits a strong departure from equilibrium and can no longer be mathematically expressed as a small perturbation by Chapman-Enskog theory. Under these conditions, the closure of the Navier-Stokes equations through the constitutive relations is no longer valid and a kinetic description is necessary.

II. CONTINUUM BREAKDOWN PARAMETERS

Continuum breakdown parameters are dimensionless quantities that are used to characterize the degree of departure from an equilibrium Maxwellian distribution and to determine when continuum breakdown has occurred. These quantities are generally compared against a continuum breakdown criterion, which relates the magnitude of the breakdown parameter for a given physical mechanism (e.g., entropy generation rate, gradients in density, velocity, temperature, etc.) to a measure of nonequilibrium [8–10]. The breakdown criterion is selected as a threshold below which macroscopic observables from both continuum and kinetic solutions are in good agreement, generally within 5% [9,11–13]. Although a number of different approaches to identify continuum breakdown have been proposed, this work focuses on continuum breakdown parameters as determined by expressions involving macroscopic quantities obtained from a CFD (Navier-Stokes) solution. Furthermore, this work adopts the breakdown criteria values established in previous investigations to facilitate comparisons with the proposed breakdown parameters and discussion herein.

Bird [8] proposed a continuum breakdown parameter for steady and unsteady expanding flows. For steady, expanding flows the parameter takes the form

$$P = \frac{\sqrt{\pi}}{2} s \frac{\lambda}{\rho} \left| \frac{d\rho}{dl} \right|. \tag{1}$$

The quantities ρ and λ are the local density and mean free path, respectively; s, the speed ratio, is given by $s = u\beta$, where u is the local velocity and β is the inverse most probable speed; and l represents the distance along a streamline.

In a later work, Bird [14] put forth the concept of a local Knudsen number based on the length scale of macroscopic gradients, for assessing the validity of the continuum approximation for a given flow system. This concept was furthered by Boyd and co-workers [9,15] to form the gradient-length-local (GLL) Knudsen number, which is one of the most widely used parameters for assessing continuum breakdown for compressing and expanding hypersonic flows based on a Navier-Stokes solution. This parameter is expressed as the ratio of the local mean free path and a length scale determined by flow gradients

$$\mathrm{Kn}_{\mathrm{GLL}} = \frac{\lambda}{Q_{\mathrm{local}}}\left|\frac{dQ}{dx}\right|, \tag{2}$$

where λ is the local mean free path and Q is a macroscopic observable such as density, velocity magnitude, or temperature, whose gradients are calculated with respect to a flow field distance. When Q is set as the velocity magnitude, $Q_{\mathrm{local}} = \max(|\boldsymbol{v}|,a)$, where a is the local sonic speed [16].

A more rigorous formulation of the continuum breakdown parameters for *steady flows* may be obtained directly from the Chapman-Enskog method, involving expansion of the velocity distribution function $f(\boldsymbol{C})$ in a small parameter, which provides the governing equations for systems that exhibit *small departures* from equilibrium. To first order in the Chapman-Enskog expansion, the distribution function $f(\boldsymbol{C})$ is expressed as the equilibrium (Maxwellian) distribution function $f^{(0)}(\boldsymbol{C})$ plus a perturbation

$$f(\boldsymbol{C}) = f^{(0)}(\boldsymbol{C})[1 + \phi^{(1)}(\boldsymbol{C})], \tag{3}$$

where $\phi^{(1)}(\boldsymbol{C})$ is the first-order Chapman-Enskog perturbation on $f^{(0)}(\boldsymbol{C})$. Upon substitution of Eq. (3) into the Boltzmann equation, a general form for the perturbation $\phi^{(1)}(\boldsymbol{C})$ for a simple (single-species, monatomic) gas is obtained [7,17]:

$$\phi^{(1)}(\boldsymbol{C}) = -\frac{1}{n}\mathbf{A}(\boldsymbol{C})\cdot\nabla\ln T - \frac{1}{n}\mathbf{B}(\boldsymbol{C}):\nabla v, \tag{4}$$

where $\mathbf{A}(\boldsymbol{C})$ and $\mathbf{B}(\boldsymbol{C})$ are vector and tensor functions of the thermal velocity $\boldsymbol{C}$. These functions appear in the definitions for the transport coefficients of viscosity μ and thermal conductivity k_{tr} as bracket integrals

$$\mu = \tfrac{1}{10}k_B T[\mathbf{B},\mathbf{B}], \tag{5}$$

$$k_{\mathrm{tr}} = \tfrac{1}{3}k_B[\mathbf{A},\mathbf{A}]. \tag{6}$$

The solution of the unknown functions $\mathbf{A}$ and $\mathbf{B}$ is typically approximated through expansion in Sonine polynomials (an exact solution may be obtained exclusively for the case of Maxwell molecules) and explicit expressions for the transport coefficients are thus obtained to first order in Sonine polynomials in terms of the Ω integrals:

$$\mu = \frac{5k_B T}{8\Omega^{(2,2)}}, \tag{7}$$

$$k_{\mathrm{tr}} = \frac{25c_{v,\mathrm{tr}}k_B T}{16\Omega^{(2,2)}}. \tag{8}$$

Upon substitution into Eq. (4), the expression for $\phi^{(1)}$ becomes

$$\begin{aligned}\phi^{(1)}(\boldsymbol{C}) = {} & (q_x\mathcal{C}_x + q_y\mathcal{C}_y + q_z\mathcal{C}_z)\left(\tfrac{2}{5}\mathcal{C}^2 - 1\right) - 2\left(\mathcal{C}_x\mathcal{C}_y\tau_{xy} + \mathcal{C}_x\mathcal{C}_z\tau_{xz} + \mathcal{C}_y\mathcal{C}_z\tau_{yz}\right)\\ & - \left(\mathcal{C}_x^2\tau_{xx} + \mathcal{C}_y^2\tau_{yy} + \mathcal{C}_z^2\tau_{zz}\right),\end{aligned} \tag{9}$$

where the quantities τ_{ij} and q_i are dimensionless quantities defined as

$$\tau_{ij} = \frac{\mu}{p}\left(\partial_j v_i + \partial_i v_j - \frac{2}{3}\partial_k v_k\delta_{ij}\right), \tag{10}$$

$$q_i = -\frac{2\beta}{p}k_{\mathrm{tr}}\partial_i T. \tag{11}$$

These dimensionless quantities, presented by Garcia and Alder [13], are the Chapman-Enskog continuum breakdown parameters for a simple (single-species, monatomic) gas and appear as the coefficients of the terms on the right-hand side of Eq. (9). The perturbation in this case is only a function of thermal velocity normalized by the most probable thermal speed, $\mathcal{C}_i = C_i/\sqrt{2k_bT/m}$. Large values for Eqs. (10) and (11) indicate that the departure from equilibrium may no longer be considered as a small perturbation and the Navier-Stokes equations are no longer valid.

The use of such breakdown parameters for problems involving high-temperature aerothermodynamics requires the assessment of continuum breakdown for gas mixtures with excited internal energy states and chemical reactions. Deschenes *et al.* [11,12] presented an extension of the GLL Knudsen number for continuum breakdown due to rotational nonequilibrium. Other high-temperature continuum breakdown mechanisms such as vibrational nonequilibrium and chemical reactions were not considered, owing to the idea that such processes occur over characteristic time scales much greater than the elastic collisional time scale. This effort formally addresses this assumption using the generalized Chapman-Enskog method from kinetic theory.

The generalized Chapman-Enskog (GCE) method introduces a formal approach for deriving the continuum breakdown parameters for problems involving fast and slow high-temperature thermochemical processes [18]. This formalism allows for the continuum breakdown parameters to be determined precisely and in a way that is consistent with the underlying governing equations employed in the CFD solver. The GCE method was employed by Stephani *et al.* [19] to derive a set of continuum breakdown parameters for chemically frozen flows. This formulation recovers the same continuum breakdown parameters by Garcia and Alder [13], but includes additional breakdown parameters for nonequilibrium characterized by diffusion fluxes and internal (rotational and vibrational) heat fluxes.

The aim of this work is to present a complete set of GCE continuum breakdown parameters for chemically reacting, steady flows. The method for rapid and slow thermochemical processes outlined by Nagnibeda and Kustova [18] is applied for one temperature, two-temperature, and three-temperature models and the corresponding sets of breakdown parameters are presented for each (Sec. III). The GCE parameters are then applied to evaluate continuum breakdown in a Mach 24 reacting air flow over a sphere and the role of chemical reactions as an indirect mechanism for continuum breakdown is assessed (Sec. IV). A detailed comparison of (i) the mathematical forms (Sec. III E) and (ii) the predicted mechanism leading to breakdown in the reacting flow simulation (Sec. IV D), between the GCE and GLL formulation is made. A summary is presented in Sec. V.

III. FORMULATION OF GCE BREAKDOWN PARAMETERS

A. Method for rapid and slow processes

In high-speed, high-temperature flows where nonequilibrium thermal and chemical processes become important, the relaxation time scales of various collisional processes (elastic and inelastic) can vary substantially. In general, relaxation times for elastic and inelastic processes relative to the characteristic time of variation of macroscopic quantities are

$$\tau_{\text{el}} \lesssim \tau_{\text{rot}} \ll \tau_{\text{vib}} < \tau_{\text{react}} \sim \theta, \tag{12}$$

where characteristic times are τ_{el} for elastic collisions, τ_{rot} and τ_{vib} for collisions with rotational and vibrational exchange, and τ_{react} for reactions (inelastic collisions). θ is the characteristic time of change in macroscopic quantities. This effectively divides collisional processes into two groups: rapid processes with time scales much smaller than θ ($\tau_{\text{rap}} \ll \theta$) and slow processes with time scales on the order of θ ($\tau_{\text{sl}} \sim \theta$).

This variability in time scales is introduced in the GCE analysis through definition of the small parameter $\epsilon = \tau/\theta$. In consideration of rapid and slow processes the kinetic equation can be written as

$$\frac{\partial f}{\partial t} + \boldsymbol{c} \cdot \nabla_{\boldsymbol{x}} f = \frac{1}{\epsilon} J^{\text{rap}} + J^{\text{sl}}. \tag{13}$$

Using this approach, the collision operator is separated into two parts, J^{rap} weighted by $1/\epsilon = \theta/\tau_{\mathrm{rap}} \gg 1$ and J^{sl} weighted by $1/\epsilon = \theta/\tau_{\mathrm{sl}} \sim O(1)$. The GCE method is then used as before to express the distribution function to first order as

$$f = f^{(0)} + \epsilon f^{(1)} = f^{(0)}(1 + \phi_{\mathrm{GCE}}). \tag{14}$$

The aim of this work is to find the GCE breakdown parameters as determined by casting ϕ_{GCE} in terms of known Navier-Stokes flux quantities. In the following sections, three different approximations are imposed on the relative time scales introduced in Eq. (12), namely, one-temperature, two-temperature, and three-temperature assumptions, to construct the appropriate set of continuum breakdown parameters for use with each of these models employed in a continuum solver.

B. One-temperature model

In the one-temperature model, the translational and internal modes are assumed to be in equilibrium with each other and are represented by a single temperature. The associated characteristic relaxation time scales are expressed as

$$\tau_{T\text{-}T} < \tau_{R\text{-}R} \lesssim \tau_{V\text{-}V} < \tau_{T\text{-}R\text{-}V} \ll \tau_{\mathrm{react}} \sim \theta, \tag{15}$$

where $\tau_{T\text{-}T}, \tau_{R\text{-}R}, \tau_{V\text{-}V}$ are the characteristic time scales for the energy exchange within each mode and $\tau_{T\text{-}R\text{-}V}$ is the time scale for the intermodal energy exchange. In the one-temperature approximation, the energy exchanges between the translational and internal energy modes are rapid processes, while the chemical reactions are on the order of the gas dynamic time scales and treated as slow processes:

$$J^{\mathrm{rap}} = J^{T\text{-}T} + J^{R\text{-}R} + J^{V\text{-}V} + J^{T\text{-}R\text{-}V}, \quad J^{\mathrm{sl}} = J^{\mathrm{react}}. \tag{16}$$

Under the one-temperature approximation, the GCE perturbation $\phi_{\mathrm{GCE},s}$ for species s is of the form [18]

$$\phi_{\mathrm{GCE},s} = -\frac{1}{n}\mathbf{A}_s \cdot \nabla \ln(T_{\mathrm{tr}}) - \frac{1}{n}\sum_t \mathbf{D}_s^t \cdot \boldsymbol{d}_t - \frac{1}{n}\mathbf{B}_s : \nabla \mathbf{v} - \frac{1}{n}F_s \nabla \cdot \mathbf{v} - \frac{1}{n}G_s. \tag{17}$$

The generalized functions $\mathbf{A}_s$ and $\mathbf{D}_s^t$ are vector functions of the reduced peculiar velocity $\boldsymbol{\mathcal{C}}_s$, $\mathbf{B}_s$ is a tensor function of $\boldsymbol{\mathcal{C}}_s$, and F_s and G_s are scalars. The second term on the right-hand side of Eq. (17) contains the term $\boldsymbol{d}_t$, which is the diffusion driving force for species t defined as

$$\boldsymbol{d}_t = \nabla\left(\frac{n_t}{n}\right) + \left(\frac{n_t}{n} - \frac{\rho_t}{\rho}\right)\nabla \ln(p). \tag{18}$$

The solutions of the unknown generalized functions are obtained as expansions in the Sonine $\mathcal{S}_\nu^n(x)$ and Waldmann-Trübenbacher $\mathcal{P}^n(x)$ polynomials with accompanying expansion coefficients (e.g., $a_{s,rpq}$):

$$\begin{aligned}
\mathbf{A}_s &= -\left(\frac{m_s}{2k_b T_{\mathrm{tr}}}\right)^{1/2} \boldsymbol{\mathcal{C}}_s \sum_{rpq} a_{s,rpq} \mathcal{S}_{3/2}^{(r)}\left(\mathcal{C}_s^2\right)\mathcal{P}^{(p)}(\varepsilon_{\mathrm{rot},s})\mathcal{P}^{(q)}(\varepsilon_{\mathrm{vib},s}),\\
\mathbf{D}_s^t &= \left(\frac{m_s}{2k_b T_{\mathrm{tr}}}\right)^{1/2} \boldsymbol{\mathcal{C}}_s \sum_{r} d_{s,r}^t \mathcal{S}_{3/2}^{(r)}\left(\mathcal{C}_s^2\right),\\
\mathbf{B}_s &= \left(\boldsymbol{\mathcal{C}}_s\boldsymbol{\mathcal{C}}_s - \frac{1}{3}\mathcal{C}_s^2\mathbb{I}\right)\sum_r b_{s,r}\mathcal{S}_{3/2}^{(r)}\left(\mathcal{C}_s^2\right),\\
F_s &= \sum_{rpq} f_{s,rpq}\mathcal{S}_{1/2}^{(r)}\left(\mathcal{C}_s^2\right)\mathcal{P}^{(p)}(\varepsilon_{\mathrm{rot},s})\mathcal{P}^{(q)}(\varepsilon_{\mathrm{vib},s}),\\
G_s &= -\sum_{rpq} g_{s,rpq}\mathcal{S}_{1/2}^{(r)}\left(\mathcal{C}_s^2\right)\mathcal{P}^{(p)}(\varepsilon_{\mathrm{rot},s})\mathcal{P}^{(q)}(\varepsilon_{\mathrm{vib},s}).
\end{aligned} \tag{19}$$

Note that all functions in Eq. (19) are expanded by polynomials in the rapid processes only, which for the single-temperature approximation include $\mathcal{C}_s$, $\varepsilon_{\mathrm{rot},s}$, and $\varepsilon_{\mathrm{vib},s}$. The transport coefficients of thermal conductivity (translational $k_{\mathrm{tr},s}$, rotational $k_{\mathrm{rot},s}$, and vibrational $k_{\mathrm{vib},s}$), viscosity (shear μ_s and bulk ζ_s), multicomponent diffusion (mass D_{st} and thermal $D_{T,s}$), and relaxation pressure ($p_{\mathrm{rel},s}$) may be expressed in terms of the expansion coefficients [18]

$$k_{\mathrm{tr},s}+k_{\mathrm{rot},s}+k_{\mathrm{vib},s}=\frac{k_b}{3}[\mathbf{A}_s,\mathbf{A}_s]\Rightarrow\begin{cases}k_{\mathrm{tr},s}=\frac{5k_b}{4}\frac{n_s}{n}a_{s,100}\\ k_{\mathrm{rot},s}=\frac{m_s c_{v,\mathrm{rot},s}}{2}\frac{n_s}{n}a_{s,010}\\ k_{\mathrm{vib},s}=\frac{m_s c_{v,\mathrm{vib},s}}{2}\frac{n_s}{n}a_{s,001},\end{cases}$$

$$D_{T,s}=\frac{1}{3n}\big[\mathbf{D}_s^t,\mathbf{A}_s\big]=-\frac{1}{2n}a_{s,000},\quad D_{\mathrm{st}}=\frac{1}{3n}\big[\mathbf{D}_s^t,\mathbf{D}_s^t\big]=\frac{1}{2n}d_{s,0}^t,$$

$$\mu_s=\frac{k_bT_{\mathrm{tr}}}{10}[\mathbf{B}_s,\mathbf{B}_s]=\frac{k_bT_{\mathrm{tr}}}{2}\frac{n_s}{n}b_{s,0},\quad \zeta_s=k_bT_{\mathrm{tr}}[F_s,F_s]=-k_bT_{\mathrm{tr}}\frac{n_s}{n}f_{s,100},$$

$$p_{\mathrm{rel},s}=k_bT_{\mathrm{tr}}[F_s,G_s]=k_bT_{\mathrm{tr}}\frac{n_s}{n}g_{s,100}. \tag{20}$$

Additional transport mechanisms are considered in this work from that of Stephani *et al.* [19]. These include the thermal component of diffusion resulting from temperature gradients, bulk viscosity that arises from inelastic intermodal (T-R-V) energy exchange (a rapid process in the single-temperature model), and the relaxation pressure, which is a result of the existence of rapid and slow inelastic processes. Chemical relaxation is the only slow process considered in this case. Substituting these transport coefficient expressions [Eq. (20)] into Eq. (19), we arrive at the final expression for the generalized functions

$$\begin{aligned}
\mathbf{A}_s&=\mathbf{A}_{s,T}+\mathbf{A}_{s,\mathrm{tr}}+\mathbf{A}_{s,\mathrm{rot}}+\mathbf{A}_{s,\mathrm{vib}},\\
\mathbf{A}_{s,T}&=\left(\frac{m_s}{2k_bT_{\mathrm{tr}}}\right)^{1/2}2nD_{T,s}\boldsymbol{\mathcal{C}}_s,\\
\mathbf{A}_{s,\mathrm{tr}}&=-\left(\frac{m_s}{2k_bT_{\mathrm{tr}}}\right)^{1/2}\frac{4K_{\mathrm{tr},s}}{5k_b}\frac{n}{n_s}\left(\frac{5}{2}-\mathcal{C}_s^2\right)\boldsymbol{\mathcal{C}}_s,\\
\mathbf{A}_{s,\mathrm{rot}}&=-\left(\frac{m_s}{2k_bT_{\mathrm{tr}}}\right)^{1/2}\frac{2K_{\mathrm{rot},s}}{m_sc_{v,\mathrm{rot},s}}\frac{n}{n_s}(\bar{\varepsilon}_{\mathrm{rot},s}-\varepsilon_{\mathrm{rot},s})\boldsymbol{\mathcal{C}}_s,\\
\mathbf{A}_{s,\mathrm{vib}}&=-\left(\frac{m_s}{2k_bT_{\mathrm{tr}}}\right)^{1/2}\frac{2K_{\mathrm{vib},s}}{m_sc_{v,\mathrm{vib},s}}\frac{n}{n_s}(\bar{\varepsilon}_{\mathrm{vib},s}-\varepsilon_{\mathrm{vib},s})\boldsymbol{\mathcal{C}}_s,\\
\mathbf{D}_s^t&=\left(\frac{m_s}{2k_bT_{\mathrm{tr}}}\right)^{1/2}2nD_{\mathrm{st}}\boldsymbol{\mathcal{C}}_s,\\
\mathbf{B}_s&=\frac{2\mu_s}{k_bT_{\mathrm{tr}}}\frac{n}{n_s}\left(\boldsymbol{\mathcal{C}}_s\boldsymbol{\mathcal{C}}_s-\frac{1}{3}\mathcal{C}_s^2\mathbb{I}\right),\\
F_s&=-\frac{\zeta_s}{k_bT_{\mathrm{tr}}}\frac{n}{n_s}\left(\frac{3}{2}-\mathcal{C}_s^2\right),\\
G_s&=\frac{p_{\mathrm{rel},s}}{k_bT_{\mathrm{tr}}}\frac{n}{n_s}\left(\frac{3}{2}-\mathcal{C}_s^2\right).
\end{aligned}\tag{21}$$

The perturbation defined in Eq. (17) can now be expressed in terms of the transport coefficients

$$
\begin{aligned}
\phi_{\mathrm{GCE},s} = {} & -\frac{1}{n}\sum_t \left(\frac{m_s}{2k_b T_{\mathrm{tr}}}\right)^{1/2} 2nD_{\mathrm{st}}\boldsymbol{\mathcal{C}}_s \cdot \boldsymbol{d}_t - \frac{1}{n}\left(\frac{m_s}{2k_b T_{\mathrm{tr}}}\right)^{1/2} 2nD_{T,s}\boldsymbol{\mathcal{C}}_s \cdot \nabla \ln(T_{\mathrm{tr}}) \\
& - \frac{1}{n}\left(\frac{m_s}{2k_b T_{\mathrm{tr}}}\right)^{1/2} \frac{4K_{\mathrm{tr},s}}{5k_b}\frac{n}{n_s}\left(\mathcal{C}_s^2 - \frac{5}{2}\right)\boldsymbol{\mathcal{C}}_s \cdot \nabla \ln(T_{\mathrm{tr}}) \\
& - \frac{1}{n}\left(\frac{m_s}{2k_b T_{\mathrm{tr}}}\right)^{1/2} \frac{2K_{\mathrm{rot},s}}{m_s c_{v,\mathrm{rot},s}}\frac{n}{n_s}(\varepsilon_{\mathrm{rot},s} - \bar{\varepsilon}_{\mathrm{rot},s})\boldsymbol{\mathcal{C}}_s \cdot \nabla \ln(T_{\mathrm{tr}}) \\
& - \frac{1}{n}\left(\frac{m_s}{2k_b T_{\mathrm{tr}}}\right)^{1/2} \frac{2K_{\mathrm{vib},s}}{m_s c_{v,\mathrm{vib},s}}\frac{n}{n_s}(\varepsilon_{\mathrm{vib},s} - \bar{\varepsilon}_{\mathrm{vib},s})\boldsymbol{\mathcal{C}}_s \cdot \nabla \ln(T_{\mathrm{tr}}) \\
& - \frac{1}{n}\frac{2\mu_s}{k_b T_{\mathrm{tr}}}\frac{n}{n_s}\left(\boldsymbol{\mathcal{C}}_s\boldsymbol{\mathcal{C}}_s - \frac{1}{3}\mathcal{C}_s^2\mathbb{I}\right) : \nabla\mathbf{v} \\
& - \frac{1}{n}\frac{\zeta_s}{k_b T_{\mathrm{tr}}}\frac{n}{n_s}\left(\mathcal{C}_s^2 - \frac{3}{2}\right)\nabla\cdot\mathbf{v} + \frac{1}{n}\frac{p_{\mathrm{rel},s}}{k_b T_{\mathrm{tr}}}\frac{n}{n_s}\left(\mathcal{C}_s^2 - \frac{3}{2}\right).
\end{aligned} \tag{22}
$$

The diffusion fluxes in the Navier-Stokes solvers are expressed in terms of the diffusion velocity, which has contributions from mass and thermal diffusion

$$
\boldsymbol{V}_s = \boldsymbol{V}_{M,s} + \boldsymbol{V}_{T,s} = -\sum_t D_{\mathrm{st}}\boldsymbol{d}_t - D_{T,s}\nabla \ln(T_{\mathrm{tr}}). \tag{23}
$$

Using Eq. (23) and introducing the pressure $p_s = n_s k_b T_{\mathrm{tr}}$, density $\rho_s = m_s n_s$, and inverse most probable thermal speed $\beta_s = \sqrt{m_s/2k_b T_{\mathrm{tr}}}$, the perturbation takes the form

$$
\begin{aligned}
\phi_{\mathrm{GCE},s} = {} & 2\beta_s \boldsymbol{V}_{M,s}\cdot\boldsymbol{\mathcal{C}}_s + 2\beta_s \boldsymbol{V}_{T,s}\cdot\boldsymbol{\mathcal{C}}_s - \frac{4\beta_s k_{\mathrm{tr},s}}{5p_s}\left(\mathcal{C}_s^2 - \frac{5}{2}\right)\boldsymbol{\mathcal{C}}_s\cdot\nabla T_{\mathrm{tr}} \\
& - \frac{2\beta_s k_{\mathrm{rot},s}}{\rho_s c_{v,\mathrm{rot},s} T_{\mathrm{tr}}}(\varepsilon_{\mathrm{rot},s} - \bar{\varepsilon}_{\mathrm{rot},s})\boldsymbol{\mathcal{C}}_s\cdot\nabla T_{\mathrm{tr}} - \frac{2\beta_s k_{\mathrm{vib},s}}{\rho_s c_{v,\mathrm{vib},s} T_{\mathrm{tr}}}(\varepsilon_{\mathrm{vib},s} - \bar{\varepsilon}_{\mathrm{vib},s})\boldsymbol{\mathcal{C}}_s\cdot\nabla T_{\mathrm{tr}} \\
& - \frac{2\mu_s}{p_s}\boldsymbol{\mathcal{C}}_s\boldsymbol{\mathcal{C}}_s : \left(\frac{1}{2}(\nabla\mathbf{v} + \nabla^T\mathbf{v}) - \frac{1}{3}\nabla\cdot\mathbf{v}\mathbb{I}\right) - \frac{\zeta_s}{p_s}\left(\mathcal{C}_s^2 - \frac{3}{2}\right)\nabla\cdot\mathbf{v} + \frac{p_{\mathrm{rel},s}}{p_s}\left(\mathcal{C}_s^2 - \frac{3}{2}\right).
\end{aligned} \tag{24}
$$

Finally, the GCE perturbation $\phi_{\mathrm{GCE},s}$ can be cast in terms of flux-based quantities that are readily available from a CFD solution

$$
\begin{aligned}
\phi_{\mathrm{GCE},s} = {} & \boldsymbol{D}_{M,s}\cdot\boldsymbol{\mathcal{C}}_s + \boldsymbol{D}_{T,s}\cdot\boldsymbol{\mathcal{C}}_s + \boldsymbol{q}_{\mathrm{tr},s}\cdot\boldsymbol{\mathcal{C}}_s\left(\mathcal{C}_s^2 - \tfrac{5}{2}\right) + \boldsymbol{q}_{\mathrm{rot},s}\cdot\boldsymbol{\mathcal{C}}_s(\varepsilon_{\mathrm{rot},s} - \bar{\varepsilon}_{\mathrm{rot},s}) \\
& + \boldsymbol{q}_{\mathrm{vib},s}\cdot\boldsymbol{\mathcal{C}}_s(\varepsilon_{\mathrm{vib},s} - \bar{\varepsilon}_{\mathrm{vib},s}) + \boldsymbol{\tau}_s : \boldsymbol{\mathcal{C}}_s\boldsymbol{\mathcal{C}}_s + P_{\mathrm{bulk},s}\left(\mathcal{C}_s^2 - \tfrac{3}{2}\right) + P_{\mathrm{rel},s}\left(\mathcal{C}_s^2 - \tfrac{3}{2}\right).
\end{aligned} \tag{25}
$$

The coefficients on the right-hand side of Eq. (25) are the GCE continuum breakdown parameters for a reacting gas mixture assuming a single-temperature model:

$$
\begin{aligned}
& \boldsymbol{D}_{M,s} = \frac{2\beta_s\rho_s\boldsymbol{V}_{M,s}}{\rho_s} = \frac{2\beta_s\boldsymbol{D}_{M,s}^{\mathrm{NS}}}{\rho_s}, \quad \boldsymbol{D}_{T,s} = \frac{2\beta_s\rho_s\boldsymbol{V}_{T,s}}{\rho_s} = \frac{2\beta_s\boldsymbol{D}_{T,s}^{\mathrm{NS}}}{\rho_s}, \\
& \boldsymbol{q}_{\mathrm{tr},s} = -\frac{4\beta_s}{5p_s}k_{\mathrm{tr},s}\nabla T_{\mathrm{tr}} = \frac{4\beta_s\boldsymbol{q}_{\mathrm{tr},s}^{\mathrm{NS}}}{5p_s}, \quad \boldsymbol{q}_{\mathrm{rot},s} = -\frac{2\beta_s}{\rho_s c_{v,\mathrm{rot},s}T_{\mathrm{tr}}}k_{\mathrm{rot},s}\nabla T_{\mathrm{tr}} = \frac{2\beta_s\boldsymbol{q}_{\mathrm{rot},s}^{\mathrm{NS}}}{\rho_s c_{v,\mathrm{rot},s}T_{\mathrm{tr}}}, \\
& \boldsymbol{q}_{\mathrm{vib},s} = -\frac{2\beta_s}{\rho_s c_{v,\mathrm{vib},s}T_{\mathrm{tr}}}k_{\mathrm{vib},s}\nabla T_{\mathrm{tr}} = \frac{2\beta_s\boldsymbol{q}_{\mathrm{vib},s}^{\mathrm{NS}}}{\rho_s c_{v,\mathrm{vib},s}T_{\mathrm{tr}}},
\end{aligned}
$$

$$\begin{aligned} \boldsymbol{\tau}_s &= \frac{2\mu_s}{p_s}\left(\frac{1}{2}(\nabla\mathbf{v}+\nabla^T\mathbf{v})-\frac{1}{3}\nabla\cdot\mathbf{v}\mathbb{I}\right)=\frac{\boldsymbol{\tau}_s^{\mathrm{NS}}}{p_s}, \\ P_{\mathrm{bulk},s} &= -\frac{1}{p_s}\zeta_s\nabla\cdot\mathbf{v}=\frac{p_{\mathrm{bulk},s}^{\mathrm{NS}}}{p_s}, \quad P_{\mathrm{rel},s}=\frac{p_{\mathrm{rel},s}^{\mathrm{NS}}}{p_s}. \end{aligned} \tag{26}$$

The GCE continuum breakdown parameters may be computed directly from the Navier-Stokes flux quantities [indicated on the far right-hand side of Eq. (26) by the superscript NS] of mass diffusion, thermal diffusion, Fourier heat fluxes (translational, rotational, and vibrational) based on gradients of a single temperature T_{tr}, viscous stress, bulk stress, and relaxation pressure due to chemical reactions.

C. Two-temperature model

In the two-temperature model, the translational and rotational energy modes are assumed to be in equilibrium and are represented by a single temperature T_{tr}. The vibrational energy exchange (V-V) is also assumed to be rapid, however the energy exchange between translational-rotational and vibrational modes (TR-V) is considered as a slow process, thus resulting in a separate vibrational temperature T_{vib}. The associated characteristic relaxation time scales are expressed as

$$\tau_{T\text{-}T} < \tau_{R\text{-}R} \lesssim \tau_{V\text{-}V} \lesssim \tau_{T\text{-}R} \ll \tau_{TR\text{-}V} < \tau_{\mathrm{react}} \sim \theta \tag{27}$$

and the rapid and slow collision operators for the kinetic equation corresponding to Eq. (13) are

$$J^{\mathrm{rap}} = J^{T\text{-}T} + J^{R\text{-}R} + J^{T\text{-}R} + J^{V\text{-}V}, \quad J^{\mathrm{sl}} = J^{TR\text{-}V} + J^{\mathrm{react}}. \tag{28}$$

For a mixture of gases following the two-temperature model with the simple harmonic oscillator approximation, the GCE perturbation $\phi_{\mathrm{GCE},s}$ is of the form [18]

$$\phi_{\mathrm{GCE},s} = -\frac{1}{n}\mathbf{A}_s\cdot\nabla\ln(T_{\mathrm{tr}}) - \frac{1}{n}\mathbf{A}_s^{(v)}\cdot\nabla\ln(T_{\mathrm{vib}}) - \frac{1}{n}\sum_t \mathbf{D}_s^t.\boldsymbol{d}_t - \frac{1}{n}\mathbf{B}_s:\nabla\mathbf{v} - \frac{1}{n}F_s\nabla\cdot\mathbf{v} - \frac{1}{n}G_s. \tag{29}$$

Since the TR-V exchanges are considered as slow processes, the perturbation in the two-temperature model has an additional term $\mathbf{A}_s^{(v)}$, associated with the gradients in the vibrational temperature. Additionally, only translational and rotational terms are present in F_s (below), which represents fast inelastic processes in the system. The definitions of the other functions in $\phi_{\mathrm{GCE},s}$ are the same as in Eq. (19). The Sonine and Waldmann-Trübenbacher polynomial expansion of the generalized functions are given by

$$\begin{aligned} \mathbf{A}_s &= -\left(\frac{m_s}{2k_bT_{\mathrm{tr}}}\right)^{1/2}\boldsymbol{\mathcal{C}}_s\sum_{rp}a_{s,rp}\mathcal{S}_{3/2}^{(r)}(\mathcal{C}_s^2)\mathcal{P}^{(p)}(\varepsilon_{\mathrm{rot},s}), \\ \mathbf{A}_s^{(v)} &= -\left(\frac{m_s}{2k_bT_{\mathrm{tr}}}\right)^{1/2}\boldsymbol{\mathcal{C}}_s\sum_{q}a_{s,q}^{(v)}\mathcal{P}^{(q)}(\varepsilon_{\mathrm{vib},s}), \\ \mathbf{D}_s^t &= \left(\frac{m_s}{2k_bT_{\mathrm{tr}}}\right)^{1/2}\boldsymbol{\mathcal{C}}_s\sum_{r}d_{s,r}^t\mathcal{S}_{3/2}^{(r)}(\mathcal{C}_s^2), \\ \mathbf{B}_s &= \left(\boldsymbol{\mathcal{C}}_s\boldsymbol{\mathcal{C}}_s-\frac{1}{3}\mathcal{C}_s^2\mathbb{I}\right)\sum_r b_{s,r}\mathcal{S}_{3/2}^{(r)}(\mathcal{C}_s^2), \\ F_s &= \sum_{rp}f_{s,rp}\mathcal{S}_{1/2}^{(r)}(\mathcal{C}_s^2)\mathcal{P}^{(p)}(\varepsilon_{\mathrm{rot},s}), \\ G_s &= -\sum_{rpq}g_{s,rpq}\mathcal{S}_{1/2}^{(r)}(\mathcal{C}_s^2)\mathcal{P}^{(p)}(\varepsilon_{\mathrm{rot},s})\mathcal{P}^{(q)}(\varepsilon_{\mathrm{vib},s}). \end{aligned} \tag{30}$$

The transport coefficients are next expressed in terms of the polynomial expansion coefficients [18]

$$
\begin{aligned}
k_{\mathrm{tr},s} + k_{\mathrm{rot},s} &= \frac{k_b}{3}[\mathbf{A}_s, \mathbf{A}_s] \Rightarrow \begin{cases} k_{\mathrm{tr},s} = \frac{5k_b}{4}\frac{n_s}{n}a_{s,10} \\ k_{\mathrm{rot},s} = \frac{m_s c_{v,\mathrm{rot},s}}{2}\frac{n_s}{n}a_{s,01}, \end{cases}\\
k_{\mathrm{vib},s} &= \frac{k_b}{3}\left[\mathbf{A}_s^{(v)}, \mathbf{A}_s^{(v)}\right] = \frac{m_s c_{v,\mathrm{vib},s}}{2}\frac{n_s}{n}a_{s,1}^{(v)},\\
D_{T,s} &= \frac{1}{3n}\left[\mathbf{D}_s^t, \mathbf{A}_s\right] = -\frac{1}{2n}a_{s,00},\\
D_{T,s}^{(v)} &= \frac{1}{3n}\left[\mathbf{D}_s^t, \mathbf{A}_s^{(v)}\right] = -\frac{1}{2n}a_{s,0}^{(v)},\\
D_{\mathrm{st}} &= \frac{1}{3n}\left[\mathbf{D}_s^t, \mathbf{D}_s^t\right] = \frac{1}{2n}d_{s,0}^t,\\
\mu_s &= \frac{k_b T_{\mathrm{tr}}}{10}[\mathbf{B}_s, \mathbf{B}_s] = \frac{k_b T_{\mathrm{tr}}}{2}\frac{n_s}{n}b_{s,0},\\
\zeta_s &= k_b T_{\mathrm{tr}}[F_s, F_s] = -k_b T_{\mathrm{tr}}\frac{n_s}{n}f_{s,10},\\
p_{\mathrm{rel},s} &= k_b T_{\mathrm{tr}}[F_s, G_s] = k_b T_{\mathrm{tr}}\frac{n_s}{n}g_{s,100}.
\end{aligned}
\tag{31}
$$

Note that there is an additional thermal diffusion coefficient, arising from the separate vibrational temperature in the two-temperature model approximation. Using the above definitions, the first-order approximation to the generalized functions can be represented in terms of the transport coefficients

$$
\begin{aligned}
\mathbf{A}_s &= \mathbf{A}_{s,T} + \mathbf{A}_{s,\mathrm{tr}} + \mathbf{A}_{s,\mathrm{rot}}, \quad \mathbf{A}_s^{(v)} = \mathbf{A}_{s,T}^{(v)} + \mathbf{A}_{s,\mathrm{vib}}^{(v)},\\
\mathbf{A}_{s,T} &= \left(\frac{m_s}{2k_b T_{\mathrm{tr}}}\right)^{1/2} 2nD_{T,s}\boldsymbol{\mathcal{C}}_s,\\
\mathbf{A}_{s,\mathrm{tr}} &= -\left(\frac{m_s}{2k_b T_{\mathrm{tr}}}\right)^{1/2}\frac{4k_{\mathrm{tr},s}}{5k_b}\frac{n}{n_s}\left(\frac{5}{2} - \mathcal{C}_s^2\right)\boldsymbol{\mathcal{C}}_s,\\
\mathbf{A}_{s,\mathrm{rot}} &= -\left(\frac{m_s}{2k_b T_{\mathrm{tr}}}\right)^{1/2}\frac{2k_{\mathrm{rot},s}}{m_s c_{v,\mathrm{rot},s}}\frac{n}{n_s}(\bar{\varepsilon}_{\mathrm{rot},s} - \varepsilon_{\mathrm{rot}})\boldsymbol{\mathcal{C}}_s,\\
\mathbf{A}_{s,T}^{(v)} &= \left(\frac{m_s}{2k_b T_{\mathrm{tr}}}\right)^{1/2} 2nD_{T,s}^{(v)}\boldsymbol{\mathcal{C}}_s,\\
\mathbf{A}_{s,\mathrm{vib}}^{(v)} &= -\left(\frac{m_s}{2k_b T_{\mathrm{tr}}}\right)^{1/2}\frac{2k_{\mathrm{vib},s}}{m_s c_{v,\mathrm{vib},s}}\frac{n}{n_s}(\bar{\varepsilon}_{\mathrm{vib},s} - \varepsilon_{\mathrm{vib}})\boldsymbol{\mathcal{C}}_s,\\
\mathbf{D}_s^t &= \left(\frac{m_s}{2k_b T_{\mathrm{tr}}}\right)^{1/2} 2nD_{\mathrm{st}}\boldsymbol{\mathcal{C}}_s,\\
\mathbf{B}_s &= \frac{2\mu_s}{k_b T_{\mathrm{tr}}}\frac{n}{n_s}\left(\boldsymbol{\mathcal{C}}_s\boldsymbol{\mathcal{C}}_s - \frac{1}{3}\mathcal{C}_s^2\mathbb{I}\right),\\
F_s &= -\frac{\zeta_s}{k_b T_{\mathrm{tr}}}\frac{n}{n_s}\left(\frac{3}{2} - \mathcal{C}_s^2\right),\\
G_s &= \frac{p_{\mathrm{rel},s}}{k_b T_{\mathrm{tr}}}\frac{n}{n_s}\left(\frac{3}{2} - \mathcal{C}_s^2\right).
\end{aligned}
\tag{32}
$$

The diffusion velocity is again introduced, which for the two-temperature model has an additional thermal diffusion term

$$\boldsymbol{V}_s = \boldsymbol{V}_{M,s} + \boldsymbol{V}_{T,s} + \boldsymbol{V}_{T,s}^{(v)} = -\sum_t D_{\mathrm{st}} \boldsymbol{d}_t - D_{T,s} \nabla \ln(T_{\mathrm{tr}}) - D_{T,s}^{(v)} \nabla \ln(T_{\mathrm{vib}}). \tag{33}$$

Expressing the diffusion terms using the diffusion velocity and following a procedure similar to the one-temperature model, the perturbation becomes

$$\begin{aligned}\phi_{\mathrm{GCE},s} = {} & 2\beta_s \boldsymbol{V}_{M,s} \cdot \boldsymbol{\mathcal{C}}_s + 2\beta_s \boldsymbol{V}_{T,s} \cdot \boldsymbol{\mathcal{C}}_s + 2\beta_s \boldsymbol{V}_{T,s}^{(v)} \cdot \boldsymbol{\mathcal{C}}_s - \frac{4\beta_s k_{\mathrm{tr},s}}{5p_s}\left(\mathcal{C}_s^2 - \frac{5}{2}\right)\boldsymbol{\mathcal{C}}_s \cdot \nabla T_{\mathrm{tr}} \\ & - \frac{2\beta_s k_{\mathrm{rot},s}}{\rho_s c_{v,\mathrm{rot},s} T_{\mathrm{tr}}}(\varepsilon_{\mathrm{rot},s} - \bar{\varepsilon}_{\mathrm{rot},s})\boldsymbol{\mathcal{C}}_s \cdot \nabla T_{\mathrm{tr}} - \frac{2\beta_s k_{\mathrm{vib},s}}{\rho_s c_{v,\mathrm{vib},s} T_{\mathrm{vib}}}(\varepsilon_{\mathrm{vib},s} - \bar{\varepsilon}_{\mathrm{vib},s})\boldsymbol{\mathcal{C}}_s \cdot \nabla T_{\mathrm{vib}} \\ & - \frac{2\mu_s}{p_s}\boldsymbol{\mathcal{C}}_s\boldsymbol{\mathcal{C}}_s : \left(\frac{1}{2}(\nabla \mathbf{v} + \nabla^T \mathbf{v}) - \frac{1}{3}\nabla \cdot \mathbf{v}\mathbb{I}\right) - \frac{\zeta_s}{p_s}\left(\mathcal{C}_s^2 - \frac{3}{2}\right)\nabla \cdot \mathbf{v} + \frac{p_{\mathrm{rel},s}}{p_s}\left(\mathcal{C}_s^2 - \frac{3}{2}\right)\end{aligned} \tag{34}$$

and the GCE perturbation $\phi_{\mathrm{GCE},s}$ for the two-temperature model is expressed in terms of flux-based quantities as

$$\begin{aligned}\phi_{\mathrm{GCE},s} = {} & \boldsymbol{D}_{M,s} \cdot \boldsymbol{\mathcal{C}}_s + \boldsymbol{D}_{T,s} \cdot \boldsymbol{\mathcal{C}}_s + \boldsymbol{D}_{T,s}^{(v)} \cdot \boldsymbol{\mathcal{C}}_s + \boldsymbol{q}_{\mathrm{tr},s} \cdot \boldsymbol{\mathcal{C}}_s\left(\mathcal{C}_s^2 - \tfrac{5}{2}\right) + \boldsymbol{q}_{\mathrm{rot},s} \cdot \boldsymbol{\mathcal{C}}_s\left(\varepsilon_{\mathrm{rot},s} - \bar{\varepsilon}_{\mathrm{rot},s}\right) \\ & + \boldsymbol{q}_{\mathrm{vib},s} \cdot \boldsymbol{\mathcal{C}}_s(\varepsilon_{\mathrm{vib},s} - \bar{\varepsilon}_{\mathrm{vib},s}) + \boldsymbol{\tau}_s : \boldsymbol{\mathcal{C}}_s\boldsymbol{\mathcal{C}}_s + P_{\mathrm{bulk},s}\left(\mathcal{C}_s^2 - \tfrac{3}{2}\right) + P_{\mathrm{rel},s}\left(\mathcal{C}_s^2 - \tfrac{3}{2}\right).\end{aligned} \tag{35}$$

Finally, the GCE continuum breakdown parameters for the case of the two-temperature model are given by

$$\begin{aligned}\boldsymbol{D}_{M,s} &= \frac{2\beta_s \rho_s \boldsymbol{V}_{M,s}}{\rho_s} = \frac{2\beta_s \boldsymbol{D}_{M,s}^{\mathrm{NS}}}{\rho_s}, \\ \boldsymbol{D}_{T,s}^{(v)} &= \frac{2\beta_s \rho_s \boldsymbol{V}_{T,s}^{(v)}}{\rho_s} = \frac{2\beta_s \boldsymbol{D}_{T,s}^{(v),\mathrm{NS}}}{\rho_s}, \\ \boldsymbol{D}_{T,s} &= \frac{2\beta_s \rho_s \boldsymbol{V}_{T,s}}{\rho_s} = \frac{2\beta_s \boldsymbol{D}_{T,s}^{\mathrm{NS}}}{\rho_s}, \\ \boldsymbol{q}_{\mathrm{tr},s} &= -\frac{4\beta_s}{5p_s} k_{\mathrm{tr},s} \nabla T_{\mathrm{tr}} = \frac{4\beta_s \boldsymbol{q}_{\mathrm{tr},s}^{\mathrm{NS}}}{5p_s}, \\ \boldsymbol{q}_{\mathrm{rot},s} &= -\frac{2\beta_s}{\rho_s c_{v,\mathrm{rot},s} T_{\mathrm{tr}}} k_{\mathrm{rot},s} \nabla T_{\mathrm{tr}} = \frac{2\beta_s \boldsymbol{q}_{\mathrm{rot},s}^{\mathrm{NS}}}{\rho_s c_{v,\mathrm{rot},s} T_{\mathrm{tr}}}, \\ \boldsymbol{q}_{\mathrm{vib},s} &= -\frac{2\beta_s}{\rho_s c_{v,\mathrm{vib},s} T_{\mathrm{vib}}} k_{\mathrm{vib},s} \nabla T_{\mathrm{vib}} = \frac{2\beta_s \boldsymbol{q}_{\mathrm{vib},s}^{\mathrm{NS}}}{\rho_s c_{v,\mathrm{vib},s} T_{\mathrm{vib}}}, \\ \boldsymbol{\tau}_s &= \frac{2\mu_s}{p_s}\left(\frac{1}{2}(\nabla \mathbf{v} + \nabla^T \mathbf{v}) - \frac{1}{3}\nabla \cdot \mathbf{v}\mathbb{I}\right) = \frac{\boldsymbol{\tau}_s^{\mathrm{NS}}}{p_s}, \\ P_{\mathrm{bulk},s} &= -\frac{1}{p_s}\zeta_s \nabla \cdot \mathbf{v} = \frac{p_{\mathrm{bulk},s}^{\mathrm{NS}}}{p_s}, \quad P_{\mathrm{rel},s} = \frac{p_{\mathrm{rel},s}^{\mathrm{NS}}}{p_s}.\end{aligned} \tag{36}$$

D. Three-temperature model

In the three-temperature model, the energy exchange between T-T, R-R, and V-V (intramodal) are considered as fast processes, while T-R-V (intermodal) energy exchange is a slow process. Owing to the fast intramodal processes, the resulting translational, rotational, and vibrational modes are assumed to follow Boltzmann distributions with distinct temperatures T_{tr}, T_{rot}, and T_{vib}, but these temperatures are not necessarily in equilibrium owing to the slow T-R-V exchange. The corresponding characteristic time scales and fast and slow collision operators are thus

$$\tau_{T\text{-}T} < \tau_{R\text{-}R} < \tau_{V\text{-}V} \ll \tau_{T\text{-}R\text{-}V} < \tau_{\mathrm{react}} \sim \theta, \tag{37}$$

$$J^{\mathrm{rap}} = J^{T\text{-}T} + J^{R\text{-}R} + J^{V\text{-}V}, \quad J^{\mathrm{sl}} = J^{T\text{-}R\text{-}V} + J^{\mathrm{react}}. \tag{38}$$

For a mixture of gases following the three-temperature model with a rigid-rotor–harmonic oscillator assumption, the GCE perturbation $\phi_{\mathrm{GCE},s}$ is of the form

$$\begin{aligned}\phi_{\mathrm{GCE},s} = &-\frac{1}{n}\mathbf{A}_s \cdot \nabla \ln(T_{\mathrm{tr}}) - \frac{1}{n}\mathbf{A}_s^{(r)} \cdot \nabla \ln(T_{\mathrm{rot}}) - \frac{1}{n}\mathbf{A}_s^{(v)} \cdot \nabla \ln(T_{\mathrm{vib}}) \\ &-\frac{1}{n}\sum_t \mathbf{D}_s^t \cdot \boldsymbol{d}_t - \frac{1}{n}\mathbf{B}_s : \nabla\mathbf{v} - \frac{1}{n}G_s. \end{aligned} \tag{39}$$

The perturbation in the three-temperature model has two new terms $\mathbf{A}_s^{(r)}$ and $\mathbf{A}_s^{(v)}$ associated with the gradients in the rotational and vibrational temperatures. Since all intermodal inelastic energy exchange processes are slow processes, the F_s term vanishes from Eq. (39). The polynomial expansion of the generalized functions are given by

$$\begin{aligned}
\mathbf{A}_s &= -\left(\frac{m_s}{2k_b T_{\mathrm{tr}}}\right)^{1/2} \boldsymbol{\mathcal{C}}_s \sum_r a_{s,r} \mathcal{S}_{3/2}^{(r)}\left(\mathcal{C}_s^2\right), \\
\mathbf{A}_s^{(r)} &= -\left(\frac{m_s}{2k_b T_{\mathrm{tr}}}\right)^{1/2} \boldsymbol{\mathcal{C}}_s \sum_p a_{s,p}^{(r)} \mathcal{P}^{(p)}(\varepsilon_{\mathrm{rot},s}), \\
\mathbf{A}_s^{(v)} &= -\left(\frac{m_s}{2k_b T_{\mathrm{tr}}}\right)^{1/2} \boldsymbol{\mathcal{C}}_s \sum_q a_{s,q}^{(v)} \mathcal{P}^{(q)}(\varepsilon_{\mathrm{vib},s}), \\
\mathbf{D}_s^t &= \left(\frac{m_s}{2k_b T_{\mathrm{tr}}}\right)^{1/2} \boldsymbol{\mathcal{C}}_s \sum_r d_{s,r}^t \mathcal{S}_{3/2}^{(r)}\left(\mathcal{C}_s^2\right), \\
\mathbf{B}_s &= \left(\boldsymbol{\mathcal{C}}_s\boldsymbol{\mathcal{C}}_s - \frac{1}{3}\mathcal{C}_s^2 \mathbb{I}\right) \sum_r b_{s,r} \mathcal{S}_{3/2}^{(r)}\left(\mathcal{C}_s^2\right), \\
G_s &= -\sum_{rpq} g_{s,rpq} \mathcal{S}_{1/2}^{(r)}\left(\mathcal{C}_s^2\right) \mathcal{P}^{(p)}(\varepsilon_{\mathrm{rot},s}) \mathcal{P}^{(q)}(\varepsilon_{\mathrm{vib},s}).
\end{aligned} \tag{40}$$

The transport coefficients are again expressed in terms of the polynomial expansion coefficients

$$\begin{aligned}
k_{\mathrm{tr},s} &= \frac{k_b}{3}[\mathbf{A}_s, \mathbf{A}_s] = \frac{5k_b}{4}\frac{n_s}{n} a_{s,1}, \\
k_{\mathrm{rot},s} &= \frac{k_b}{3}\left[\mathbf{A}_s^{(r)}, \mathbf{A}_s^{(r)}\right] = \frac{m_s c_{v,\mathrm{rot},s}}{2}\frac{n_s}{n} a_{s,1}^{(r)}, \\
k_{\mathrm{vib},s} &= \frac{k_b}{3}\left[\mathbf{A}_s^{(v)}, \mathbf{A}_s^{(v)}\right] = \frac{m_s c_{v,\mathrm{vib},s}}{2}\frac{n_s}{n} a_{s,1}^{(v)}, \\
D_{T,s} &= \frac{1}{3n}\left[\mathbf{D}_s^t, \mathbf{A}_s\right] = -\frac{1}{2n} a_{s,0}, \\
D_{T,s}^{(r)} &= \frac{1}{3n}\left[\mathbf{D}_s^t, \mathbf{A}_s^{(r)}\right] = -\frac{1}{2n} a_{s,0}^{(r)}, \\
D_{T,s}^{(v)} &= \frac{1}{3n}\left[\mathbf{D}_s^t, \mathbf{A}_s^{(v)}\right] = -\frac{1}{2n} a_{s,0}^{(v)},
\end{aligned}$$

$$\begin{aligned} D_{\mathrm{st}} &= \frac{1}{3n}\big[\mathbf{D}_s^t,\mathbf{D}_s^t\big] = \frac{1}{2n}d_{s,0}^t, \\ \mu_s &= \frac{k_b T_{\mathrm{tr}}}{10}[\mathbf{B}_s,\mathbf{B}_s] = \frac{k_b T_{\mathrm{tr}}}{2}\frac{n_s}{n}b_{s,0}, \\ \zeta_s &= k_b T_{\mathrm{tr}}[F_s,F_s] = 0, \\ p_{\mathrm{rel},s} &= k_b T_{\mathrm{tr}}[F_s,G_s] = 0. \end{aligned} \tag{41}$$

Note that in the three-temperature model, there are two additional thermal diffusion coefficients, arising from the separate rotational and vibrational temperatures. The bulk viscosity ζ and the relaxation pressure p_{rel} are equal to zero in this case due to the fact that there are no fast intermodal inelastic processes. The perturbation function is next expressed in terms of the transport coefficients to obtain

$$\begin{aligned} \mathbf{A}_s &= \mathbf{A}_{s,T} + \mathbf{A}_{s,\mathrm{tr}}, \quad \mathbf{A}_s^{(r)} = \mathbf{A}_{s,T}^{(r)} + \mathbf{A}_{s,\mathrm{rot}}^{(r)}, \quad \mathbf{A}_s^{(v)} = \mathbf{A}_{s,T}^{(v)} + \mathbf{A}_{s,\mathrm{vib}}^{(v)}, \\ \mathbf{A}_{s,T} &= \left(\frac{m_s}{2k_b T_{\mathrm{tr}}}\right)^{1/2} 2nD_{T,s}\boldsymbol{\mathcal{C}}_s, \quad \mathbf{A}_{s,\mathrm{tr}} = -\left(\frac{m_s}{2k_b T_{\mathrm{tr}}}\right)^{1/2} \frac{4k_{\mathrm{tr},s}}{5k_b}\frac{n}{n_s}\left(\frac{5}{2} - \mathcal{C}_s^2\right)\boldsymbol{\mathcal{C}}_s, \\ \mathbf{A}_{s,T}^{(r)} &= \left(\frac{m_s}{2k_b T_{\mathrm{tr}}}\right)^{1/2} 2nD_{T,s}^{(r)}\boldsymbol{\mathcal{C}}_s, \\ \mathbf{A}_{s,\mathrm{rot}}^{(r)} &= -\left(\frac{m_s}{2k_b T_{\mathrm{tr}}}\right)^{1/2} \frac{2k_{\mathrm{rot},s}}{m_s c_{v,\mathrm{rot},s}}\frac{n}{n_s}(\bar{\varepsilon}_{\mathrm{rot},s} - \varepsilon_{\mathrm{rot}})\boldsymbol{\mathcal{C}}_s, \\ \mathbf{A}_{s,T}^{(v)} &= \left(\frac{m_s}{2k_b T_{\mathrm{tr}}}\right)^{1/2} 2nD_{T,s}^{(v)}\boldsymbol{\mathcal{C}}_s, \\ \mathbf{A}_{s,\mathrm{vib}}^{(v)} &= -\left(\frac{m_s}{2k_b T_{\mathrm{tr}}}\right)^{1/2} \frac{2k_{\mathrm{vib},s}}{m_s c_{v,\mathrm{vib},s}}\frac{n}{n_s}(\bar{\varepsilon}_{\mathrm{vib},s} - \varepsilon_{\mathrm{vib}})\boldsymbol{\mathcal{C}}_s, \\ \mathbf{D}_s^t &= \left(\frac{m_s}{2k_b T_{\mathrm{tr}}}\right)^{1/2} 2nD_{\mathrm{st}}\boldsymbol{\mathcal{C}}_s, \\ \mathbf{B}_s &= \frac{2\mu_s}{k_b T_{\mathrm{tr}}}\frac{n}{n_s}\left(\boldsymbol{\mathcal{C}}_s\boldsymbol{\mathcal{C}}_s - \frac{1}{3}\mathcal{C}_s^2\mathbb{I}\right), \\ G_s &= \frac{p_{\mathrm{rel},s}}{k_b T_{\mathrm{tr}}}\frac{n}{n_s}\left(\frac{3}{2} - \mathcal{C}_s^2\right). \end{aligned} \tag{42}$$

The diffusion velocity in the three-temperature model has four components owing to the mass diffusion and thermal diffusion from three temperature gradients

$$\begin{aligned} \boldsymbol{V}_s &= \boldsymbol{V}_{M,s} + \boldsymbol{V}_{T,s} + \boldsymbol{V}_{T,s}^{(r)} + \boldsymbol{V}_{T,s}^{(v)} \\ &= -\sum_t D_{\mathrm{st}}\boldsymbol{d}_t - D_{T,s}\nabla\ln(T_{\mathrm{tr}}) - D_{T,s}^{(r)}\nabla\ln(T_{\mathrm{rot}}) - D_{T,s}^{(v)}\nabla\ln(T_{\mathrm{vib}}). \end{aligned} \tag{43}$$

Expressing the diffusion terms using the diffusion velocity, the perturbation can be expressed as

$$\begin{aligned} \phi_{\mathrm{GCE},s} = {} & 2\beta_s\boldsymbol{V}_{M,s}\cdot\boldsymbol{\mathcal{C}}_s + 2\beta_s\boldsymbol{V}_{T,s}\cdot\boldsymbol{\mathcal{C}}_s + 2\beta_s\boldsymbol{V}_{T,s}^{(r)}\cdot\boldsymbol{\mathcal{C}}_s + 2\beta_s\boldsymbol{V}_{T,s}^{(v)}\cdot\boldsymbol{\mathcal{C}}_s \\ & - \frac{4\beta_s k_{\mathrm{tr},s}}{5p_s}\left(\mathcal{C}_s^2 - \frac{5}{2}\right)\boldsymbol{\mathcal{C}}_s\cdot\nabla T_{\mathrm{tr}} - \frac{2\beta_s k_{\mathrm{rot},s}}{\rho_s c_{v,\mathrm{rot},s}T_{\mathrm{rot}}}(\varepsilon_{\mathrm{rot},s} - \bar{\varepsilon}_{\mathrm{rot},s})\boldsymbol{\mathcal{C}}_s\cdot\nabla T_{\mathrm{rot}} \\ & - \frac{2\beta_s k_{\mathrm{vib},s}}{\rho_s c_{v,\mathrm{vib},s}T_{\mathrm{vib}}}(\varepsilon_{\mathrm{vib},s} - \bar{\varepsilon}_{\mathrm{vib},s})\boldsymbol{\mathcal{C}}_s\cdot\nabla T_{\mathrm{vib}} - \frac{2\mu_s}{p_s}\boldsymbol{\mathcal{C}}_s\boldsymbol{\mathcal{C}}_s : \left(\frac{1}{2}(\nabla\mathbf{v} + \nabla^T\mathbf{v}) - \frac{1}{3}\nabla\cdot\mathbf{v}\mathbb{I}\right). \end{aligned} \tag{44}$$

The GCE perturbation $\phi_{\mathrm{GCE},s}$ for the three-temperature model is expressed in terms of flux-based quantities as

$$\begin{aligned}\phi_{\mathrm{GCE},s} = {} & \boldsymbol{D}_{M,s}\cdot\boldsymbol{\mathcal{C}}_s + \boldsymbol{D}_{T,s}\cdot\boldsymbol{\mathcal{C}}_s + \boldsymbol{D}_{T,s}^{(r)}\cdot\boldsymbol{\mathcal{C}}_s + \boldsymbol{D}_{T,s}^{(v)}\cdot\boldsymbol{\mathcal{C}}_s + \boldsymbol{q}_{\mathrm{tr},s}\cdot\boldsymbol{\mathcal{C}}_s\left(\mathcal{C}_s^2-\tfrac{5}{2}\right)\\ & + \boldsymbol{q}_{\mathrm{rot},s}\cdot\boldsymbol{\mathcal{C}}_s(\varepsilon_{\mathrm{rot},s}-\bar{\varepsilon}_{\mathrm{rot},s}) + \boldsymbol{q}_{\mathrm{vib},s}\cdot\boldsymbol{\mathcal{C}}_s(\varepsilon_{\mathrm{vib},s}-\bar{\varepsilon}_{\mathrm{vib},s}) + \boldsymbol{\tau}_s:\boldsymbol{\mathcal{C}}_s\boldsymbol{\mathcal{C}}_s.\end{aligned}\tag{45}$$

Thus the GCE continuum breakdown parameters for the three-temperature model are

$$\begin{aligned}\boldsymbol{D}_{M,s} &= \frac{2\beta_s\rho_s\boldsymbol{V}_{M,s}}{\rho_s} = \frac{2\beta_s\boldsymbol{D}_{M,s}^{\mathrm{NS}}}{\rho_s},\\ \boldsymbol{D}_{T,s} &= \frac{2\beta_s\rho_s\boldsymbol{V}_{T,s}}{\rho_s} = \frac{2\beta_s\boldsymbol{D}_{T,s}^{\mathrm{NS}}}{\rho_s},\\ \boldsymbol{D}_{T,s}^{(r)} &= \frac{2\beta_s\rho_s\boldsymbol{V}_{T,s}^{(r)}}{\rho_s} = \frac{2\beta_s\boldsymbol{D}_{T,s}^{(r),\mathrm{NS}}}{\rho_s},\\ \boldsymbol{D}_{T,s}^{(v)} &= \frac{2\beta_s\rho_s\boldsymbol{V}_{T,s}^{(v)}}{\rho_s} = \frac{2\beta_s\boldsymbol{D}_{T,s}^{(v),\mathrm{NS}}}{\rho_s},\\ \boldsymbol{q}_{\mathrm{tr},s} &= -\frac{4\beta_s}{5p_s}k_{\mathrm{tr},s}\nabla T_{\mathrm{tr}} = \frac{4\beta_s\boldsymbol{q}_{\mathrm{tr},s}^{\mathrm{NS}}}{5p_s},\\ \boldsymbol{q}_{\mathrm{rot},s} &= -\frac{2\beta_s}{\rho_s c_{v,\mathrm{rot},s}T_{\mathrm{rot}}}k_{\mathrm{rot},s}\nabla T_{\mathrm{rot}} = \frac{2\beta_s\boldsymbol{q}_{\mathrm{rot},s}^{\mathrm{NS}}}{\rho_s c_{v,\mathrm{rot},s}T_{\mathrm{rot}}},\\ \boldsymbol{q}_{\mathrm{vib},s} &= -\frac{2\beta_s}{\rho_s c_{v,\mathrm{vib},s}T_{\mathrm{vib}}}k_{\mathrm{vib},s}\nabla T_{\mathrm{vib}} = \frac{2\beta_s\boldsymbol{q}_{\mathrm{vib},s}^{\mathrm{NS}}}{\rho_s c_{v,\mathrm{vib},s}T_{\mathrm{vib}}},\\ \boldsymbol{\tau}_s &= \frac{2\mu_s}{p_s}\left(\frac{1}{2}(\nabla\mathbf{v}+\nabla^T\mathbf{v})-\frac{1}{3}\nabla\cdot\mathbf{v}\mathbb{I}\right) = \frac{\boldsymbol{\tau}_s^{\mathrm{NS}}}{p_s}.\end{aligned}\tag{46}$$

E. Comparison with the Kn$_{\mathrm{GLL}}$ breakdown parameters

In this section, an analytical comparison between the GCE and GLL continuum breakdown parameters is made. The comparison is limited to the translational heat flux and self-diffusion flux for a single species gas. As will be seen in Sec. IV, these are the primary mechanisms leading to breakdown in the reacting flow case presented in this work, but this analysis can be readily extended to facilitate comparison between other breakdown parameter quantities.

1. *Translational heat flux*

The GCE and GLL breakdown parameters that predict continuum breakdown associated with large gradients in translational temperature (i.e., heat flux) are the translational heat flux breakdown parameter (GCE) and the GLL Knudsen number based on translational temperature [repeated from Eqs. (46) and (2)]:

$$\boldsymbol{q}_{\mathrm{tr,GCE}} = -\frac{4\beta}{5p}k_{\mathrm{tr}}\nabla T_{\mathrm{tr}},\tag{47}$$

$$\mathrm{Kn}_{\mathrm{GLL}}^{T,\mathrm{tr}} = \frac{\lambda}{T}\nabla T_{\mathrm{tr}}.\tag{48}$$

Substituting $\beta = \sqrt{m/2k_bT_{\mathrm{tr}}}$ and $p = nk_bT_{\mathrm{tr}}$ and expressing both the translational thermal conductivity and mean free path of a single-species gas in terms of Ω integrals,

$$k_{\mathrm{tr}} = \frac{25c_{v,\mathrm{tr}}k_bT_{\mathrm{tr}}}{16\Omega^{(2,2)}}, \tag{49}$$

$$\lambda = \frac{1}{n\Omega^{(2,2)}}\sqrt{\frac{2k_bT_{\mathrm{tr}}}{\pi m}}, \tag{50}$$

the ratio of the breakdown parameters is determined as

$$\frac{\boldsymbol{q}_{\mathrm{tr,GCE}}}{Kn_{\mathrm{GLL}}^{T,\mathrm{tr}}} = \frac{15\sqrt{\pi}}{16}. \tag{51}$$

This ratio indicates that the GCE and GLL continuum breakdown parameters associated with translational temperature gradients are not equivalent, but are different by a constant factor of $15\sqrt{\pi}/16$ ($\approx$1.66). This factor is precisely the normalization constant that originates from the Sonine polynomial integration during the evaluation of the bracket integral $[\mathbf{A},\mathbf{A}]$, i.e., a result from kinetic theory. It should be noted that this ratio becomes significantly more complex for a gas mixture, as Eq. (49) becomes a system of equations involving mixture composition [7].

2. *Self-diffusion flux*

The GCE and GLL breakdown parameters that predict continuum breakdown associated with large gradients in species concentration (i.e., diffusion flux) are the diffusion flux breakdown parameter (GCE) and the GLL Knudsen number based on species density:

$$\boldsymbol{D}_{M,s} = 2\beta\boldsymbol{V}_{M,s} = 2\beta D_{ss}\boldsymbol{d}_s, \tag{52}$$

$$\mathrm{Kn}_{\mathrm{GLL}}^{\rho_s} = \frac{\lambda}{\rho_s}\nabla\rho_s. \tag{53}$$

Self-diffusion is presented here to facilitate comparison, as the analysis becomes increasingly more complex for multicomponent diffusion in gas mixtures. For the case of self-diffusion, the diffusion coefficient and the driving force can be expressed as

$$D_{ss} = \frac{3k_bT_{\mathrm{tr}}}{8nm\Omega^{(1,1)}}, \tag{54}$$

$$\boldsymbol{d}_s = \frac{\nabla\rho_s}{\rho_s}. \tag{55}$$

Substituting these expressions and the definition of λ from Eq. (50), the ratio of the breakdown parameters is obtained as

$$\frac{\boldsymbol{D}_{M,s}}{\mathrm{Kn}_{\mathrm{GLL}}^{\rho_s}} = \frac{3\sqrt{\pi}}{8}\frac{\Omega^{(2,2)}}{\Omega^{(1,1)}}. \tag{56}$$

The GCE and GLL diffusion breakdown parameters are also not equivalent, but in this case their ratio is a variable function of the $\Omega^{(1,1)}$ and $\Omega^{(2,2)}$ collision integrals. This is due to the fact that diffusion, which appears in the GCE parameter, is associated with the transport of mass or identity (represented by $\Omega^{(1,1)}$), while the mean free path, which appears in the GLL parameter, is associated with the transport of momentum or energy (represented by $\Omega^{(2,2)}$). The factor of $3\sqrt{\pi}/8$ appearing on the right-hand side of Eq. (56) is the normalization constant associated with the bracket integral of $[\mathbf{D}_s^t,\mathbf{D}_s^t]$, again a result from kinetic theory. This suggests that the GLL breakdown parameters, which are expressed in terms of a Knudsen number based on a length scale determined by flow gradients [9], does not properly capture the true departure of the distribution function from equilibrium as determined by the GCE method (a precursor to the Navier-Stokes equations) and kinetic theory.

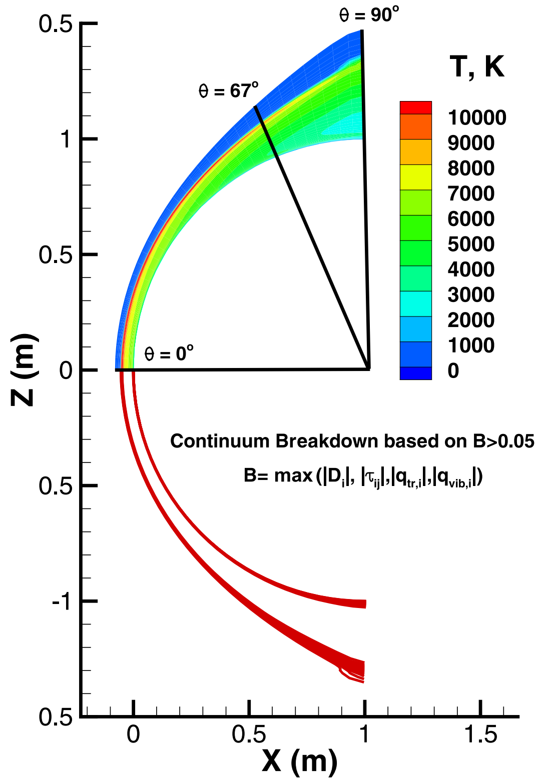

FIG. 1. Computational domain: temperature contours (top) and GCE continuum breakdown regions based on a threshold of 0.05 (bottom). Black lines indicate flow field profiles extracted for analysis at $\theta = 0°$, $67°$, and $90°$.

IV. ASSESSMENT OF CONTINUUM BREAKDOWN

The GCE breakdown parameters developed in the preceding sections are analyzed for a hypersonic flow past a sphere. Translational and vibrational heat flux, species diffusion, and stress tensor breakdown parameters are evaluated at each point in the flow field to determine the mechanisms responsible for continuum breakdown at a given location. The GCE breakdown parameters are then compared with the corresponding GLL parameters to elucidate (i) the spatial variation, if any, in the predicted onset of continuum breakdown and (ii) the physical mechanisms responsible for continuum breakdown in either case. Furthermore, the relative strengths of competing mechanisms are assessed to identify the physical processes that drive the system towards nonequilibrium and collisional processes that work to restore equilibrium.

A. Computational setup

Two-dimensional, reacting air flow past a sphere is simulated using the finite volume, implicit Langley aerothermodynamic upwind relaxation algorithm (LAURA) (Fig. 1) [20,21]. The system is modeled as an 11-species air mixture with freestream conditions as shown in Table I. The sphere surface is treated as a fully catalytic wall with radiative equilibrium wall temperature. A no-slip velocity boundary condition is enforced on the sphere surface. Chemical reactions are modeled using Park's finite rate chemistry for the entire flow field. The two-temperature model is used in which the rotational and translational modes are assumed to be in equilibrium and translational-vibrational nonequilibrium is modeled via the Landau-Teller formulation. Specieswise diffusion coefficients

TABLE I. Free stream conditions.

Parameter	Value
M	24
ρ	1×10^{-4} (kg/m^3)
T	276 (K)
u	8000 (m/s)
χ_{N_2}	0.7835
χ_{O_2}	0.2165

are obtained from the self-consistent effective binary diffusion (SCEBD) model [22,23] and mixture viscosity and translational and internal thermal conductivities are obtained from the Gupta-Yos mixing rule [24].

B. The GCE continuum breakdown

The focus of this analysis is aimed toward an understanding of the breakdown mechanisms in the shock region and near the sphere surface. The breakdown parameters for a two-temperature model presented in Sec. III C are assessed along profiles at $\theta = 0^\circ$, 67°, and 90° (Fig. 1), starting from just upstream of the bow shock and extending to the surface of the sphere. Both the normal and tangential components of the breakdown parameters are computed at each angular position. The diffusion breakdown parameter is evaluated for each component of the 11-species air mixture according to the SCEBD formulation of species diffusion flux [22]. However, it should be noted that multicomponent diffusion breakdown parameters should be computed if the pairwise diffusion coefficients are available. The translational and vibrational heat flux and stress tensor breakdown parameters have been calculated for the mixture as a whole, but these quantities may also be computed per species. The LAURA solver does not include thermal diffusion, bulk viscosity, or relaxation pressure in the governing equations, so these are omitted from the current analysis. Thus, the continuum breakdown parameters computed for this problem include

$$B = \max\left(\left|D_i^s\right|, \left|\tau_{ij}\right|, \left|q_i^{\mathrm{tr}}\right|, \left|q_i^{\mathrm{vib}}\right|\right), \tag{57}$$

each evaluated in terms of the wall-normal and tangential components. The breakdown criterion of $B = 0.05$ is adopted from the $\mathrm{Kn}_{\mathrm{GLL}}$ criterion for this analysis to facilitate comparison [9]. The continuum breakdown parameters are plotted from Figs. 2 to 4 as a function of wall-normal distance at each angular position. The shaded regions in each figure indicate regions of GCE continuum breakdown based on the definition in Eq. (57), which include breakdown within the shock region and the near-surface region, where gradients and consequently the fluxes are highest.

1. Heat flux breakdown

The wall-normal and tangential components of the translational and vibrational heat flux breakdown parameters are shown in Fig. 2 along $\theta = 0^\circ$, 67°, and 90°. Following the profiles from left (freestream) to right (sphere wall), the first shaded region represents the noncontinuum region at the shock and the second indicates the presence of a noncontinuum region near the sphere surface. Along the $\theta = 90^\circ$ profile, a third postshock breakdown region is observed due to high diffusion fluxes of NO and O_2 and will be discussed in the next section. Within each of these regions, at least one of the continuum breakdown parameters has crossed the breakdown threshold of 0.05, indicating that a kinetic scheme must be employed to accurately describe the flow field.

Along all the three angular positions considered, namely, $\theta = 0^\circ$, 67°, and 90°, the heat flux parameters initiate continuum breakdown at the shock region. Thus, within the shock, the steep gradients in the translational and vibrational temperatures and the resulting heat fluxes are responsible

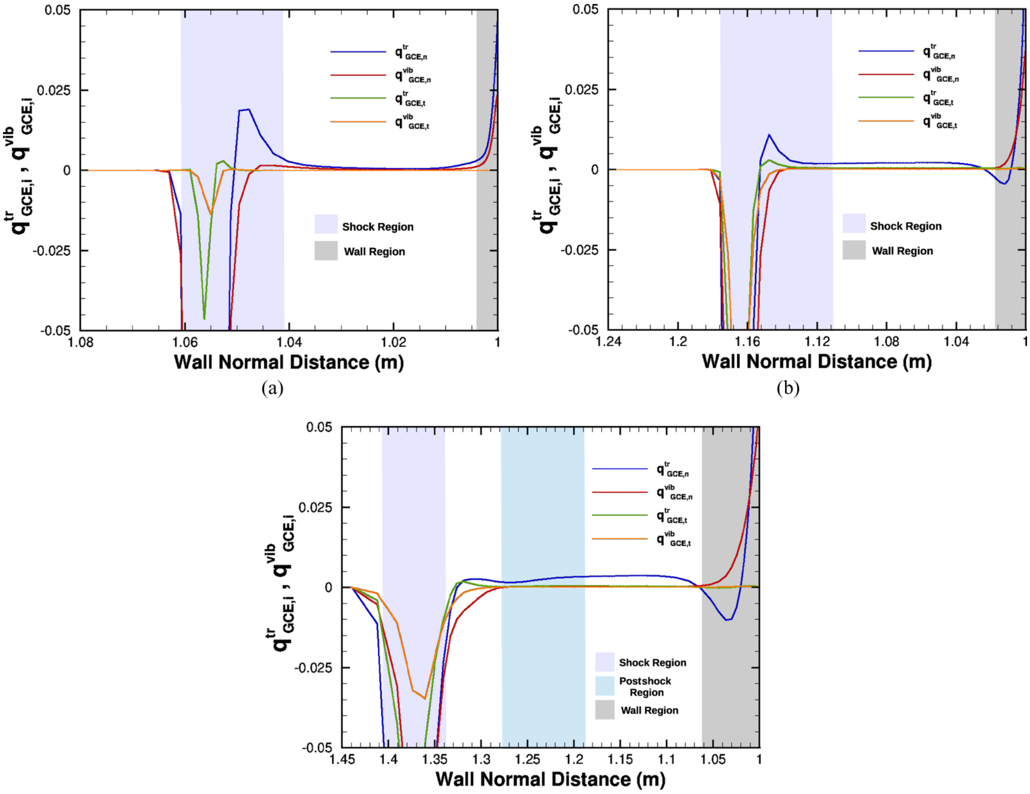

(a)

(b)

(c)

FIG. 2. Translational and vibrational heat flux breakdown parameters along (a) $\theta = 0^\circ$ (stagnation line), (b) $\theta = 67^\circ$, and (c) $\theta = 90^\circ$ profiles as indicated in Fig. 1. Note the variation in the range of the wall-normal distance from (a) to (c). The shaded regions indicate continuum breakdown as specified in Eq. (57).

for perturbing the equilibrium Maxwellian VDF of the system. The end-of-shock breakdown location marks the end of the shaded region around the shock, after which all breakdown parameters are within the breakdown threshold, and the Navier-Stokes equations may be used to compute system properties until the start of the next breakdown region is encountered. The end of shock is indicated by the specieswise diffusion breakdown parameter along each angular position considered (Table II).

Along the $\theta = 0^\circ$ and 67° locations, the continuum region beyond the end-of-shock location extends until ~ 4 and $\sim$17 mm upstream of the sphere surface, respectively. Similarly, in the case of the $\theta = 90^\circ$ position, the continuum region downstream of the postshock region [Fig. 2(c)] terminates when breakdown is observed near the sphere surface. Along all three angular positions, the near wall breakdown is determined by the specieswise diffusion fluxes, as discussed in the following section. Although the heat flux parameters do not determine the onset of breakdown near the wall, the normal components of the translational and vibrational heat flux breakdown parameters do cross the breakdown threshold very close to the sphere surface, along the $\theta = 67^\circ$ and 90° positions. The sharp temperature gradients that are set up due to the hot gases from the shock layer approaching the relatively cool sphere surface are responsible for this effect.

Further, Fig. 2 also reveals that with increasing angular positions, the near wall breakdown of the heat flux parameter occurs further upstream of the sphere surface. Since the heat flux breakdown parameters are normalized by pressure [Eq. (36)], this trend observed in the breakdown location of

TABLE II. Breakdown mechanisms: two-dimensional flow over a sphere.

Angle	Start-shock region	End-of-shock region	Wall region
0	q_n^{tr}, q_n^{vib}, D_n^{O}, D_n^{N}	$D_n^{\mathrm{O_2}}$	$D_n^{\mathrm{O_2}}$, D_n^{NO}
67	q_n^{tr}, q_n^{vib}, D_n^{O}, D_n^{NO}	$D_n^{\mathrm{O_2}}$	$D_n^{\mathrm{O_2}}$, D_n^{NO}
90	q_n^{tr}	D_n^{O}, D_n^{NO}	$D_n^{\mathrm{O_2}}$

the heat flux terms is likely due to the decreasing pressure near the sphere surface with increasing angular position, from the stagnation line ($\theta = 0^\circ$) to the sphere shoulder ($\theta = 90^\circ$).

2. *Diffusion breakdown*

Figure 3 shows the GCE diffusion breakdown parameters along $\theta = 0^\circ$, 67°, and 90°. The most prominent diffusion breakdown parameters are the wall normal components for N_2, O_2, N, O, and NO, while the tangential components (not shown) are not significant in determining any breakdown location. For similar reasons, the diffusion breakdown parameters of charged species have not been shown.

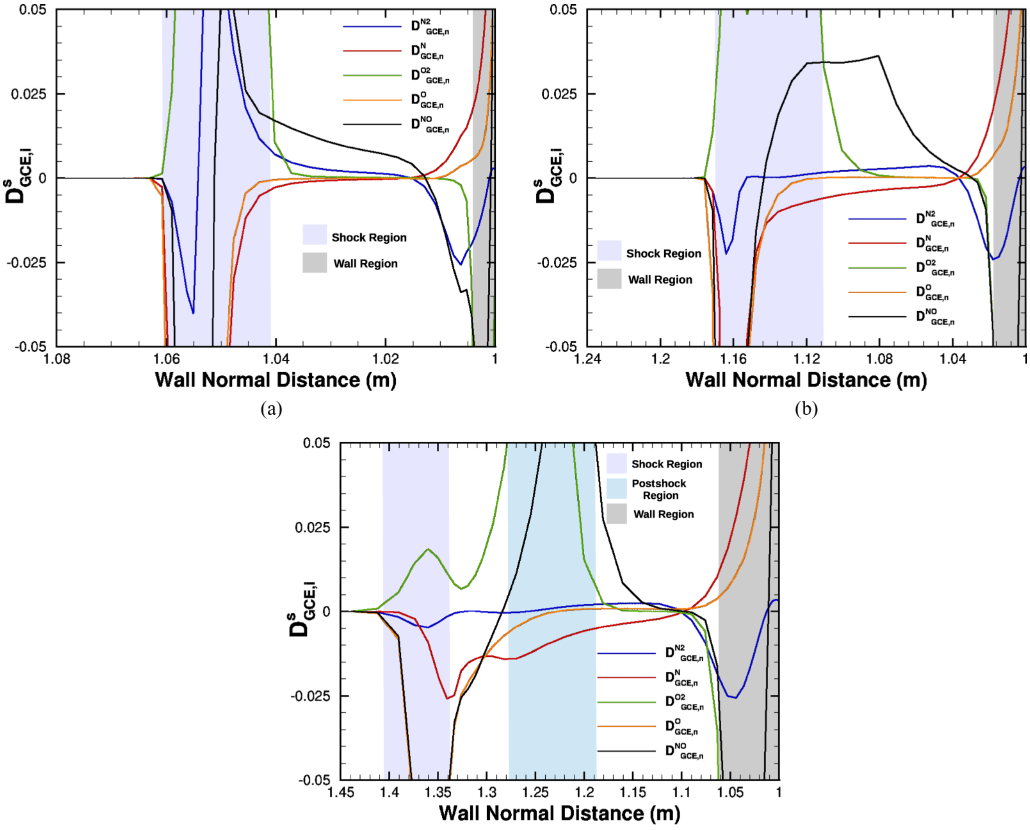

(a) (b)

(c)

FIG. 3. Diffusion breakdown parameters along (a) $\theta = 0^\circ$ (stagnation line), (b) $\theta = 67^\circ$, and (c) $\theta = 90^\circ$ profiles indicated in Fig. 1. Note the variation in the range of the wall-normal distance from (a) to (c). The shaded regions indicate continuum breakdown as specified in Eq. (57).

The diffusion flux required to compute the species-wise diffusion breakdown parameter has been evaluated using the SCEBD model of Ramshaw [22]. The diffusion breakdown parameter [Eq. (36)] is computed as the species diffusion flux normalized by the inverse most probable speed of the species and the species density, ρ_s. In case of a chemically reacting flow with conditions enabling complete dissociation and recombination, the ρ_s falls to very low values at certain locations in the flow field. This leads to mathematical anomalies in the computation of $D^s_{\mathrm{GCE},i}$. To overcome this, the ρ_s in Eq. (36) is set to $\max(\rho_s, 0.001 * \rho_{\mathrm{total}})$ where ρ_{total} is the total density at the location under consideration.

Following the $\theta = 0^\circ$ and $\theta = 67^\circ$ profile from left (free stream) to right (toward the surface), Figs. 3(a) and 3(b) indicate that diffusion fluxes have become significant at the start of shock breakdown location. However, at the sphere shoulder ($\theta = 90^\circ$), diffusion fluxes become significant only after continuum breakdown has already been initiated by the heat flux parameters [Fig. 2(c)]. The ‘end-of-shock’ breakdown location along all three angular positions is governed by the diffusion breakdown parameter. Steep species concentration gradients are observed in the shock. These gradients, coupled with the rise in pressure that accompanies the shock, contribute to the diffusion driving force [Eq. (18)] that is responsible for distorting the Maxwellian VDF of the system by means of large species diffusion fluxes. Further, the decreasing shock strength with increasing angular positions cause reactions to occur until downstream of the shock. This results in extending the ‘end-of-shock’ breakdown location further downstream of the actual shock. The postshock breakdown region that is observed along $\theta = 90^\circ$ is likely to develop due to the same reason.

In approaching the sphere surface, it is the species diffusion breakdown parameter ($D^{O_2}_{\mathrm{GCE},n}$) that determines the onset of the near wall breakdown region. The movement of hot fluid towards the relatively cold sphere surface creates temperature gradients that initiate gas phase reactions. Coupled with wall catalycity effects, steep concentration gradients develop that lead to large diffusion fluxes. Although recombinations of N begin further upstream of the wall along all three angular positions, the diffusion fluxes of O_2 determine the start of the near wall breakdown region. Unlike N_2, O_2 is almost completely dissociated in the shock. Therefore the concentration of O_2 in moving towards the wall is very low. The low concentration along with the rise in diffusion flux of O_2 due to chemical reactions in the wall vicinity, distort the VDF, leading to continuum breakdown.

Fig. 3 also reveals that with increasing angular positions, the near wall breakdown of the species-wise diffusion parameter occurs at larger distances upstream of the sphere surface. This can be attributed to the decreasing total density (and hence, species density) as one traverses along the sphere surface from the stagnation line to the sphere shoulder.

3. *Stress tensor breakdown*

Fig. 4 shows the normal (*nn*), tangential (*tt*) and shear (*nt*) stress breakdown parameters along $\theta = 0^\circ$, 67°, and 90°. Following the profiles from left to right, it can be seen that continuum breakdown occurs at the shock region before the stress components become significant. With an increase in the angular position, the value of the stress tensor components close to the sphere wall begins to increase. The sharp velocity gradients developed due to the slowing of the fluid in the wall boundary layer are responsible for this rise. However, the stress tensor breakdown parameters do not determine any of the breakdown locations.

It is clear from Figs. 2 to 4 that there exist two (three for $\theta = 90^\circ$) distinct continuum breakdown regions (shock, postshock, and near the sphere surface) where a transition needs to be made from a CFD to a kinetics-based solution technique. This transition, often referred to as the hybrid interface location introduced in Sec. I, is determined by the location where any of the breakdown parameter values has exceeded the breakdown threshold. The physical mechanisms leading to the onset of continuum breakdown are summarized in Table II for the cases considered above. The shock (and postshock) region is bound by two separate hybrid interfaces, one defining the start-of-shock continuum breakdown location and the second, defining the end-of-shock continuum breakdown location, while the breakdown near the sphere surface is governed by a single hybrid interface.

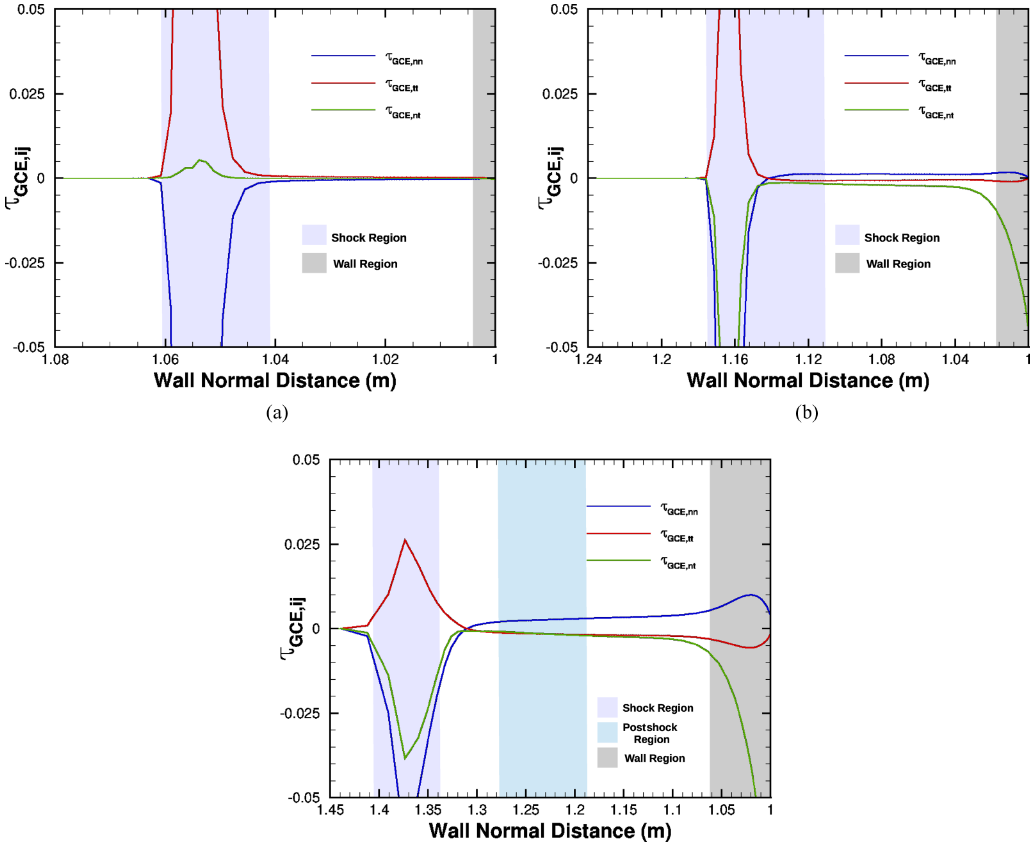

(a) (b) (c)

FIG. 4. Stress Tensor breakdown parameters along: (a) $\theta = 0^\circ$ (stagnation line), (b) $\theta = 67^\circ$, (c) $\theta = 90^\circ$ profiles indicated in Fig. 1. Note the variation in the range of the wall-normal distance from (a) to (c). The shaded regions indicate continuum breakdown as specified in Eq. (57).

Multiple breakdown parameters are listed for cases where multiple mechanisms simultaneously predict continuum breakdown. For the postshock breakdown region developed along $\theta = 90^\circ$, the interfaces are governed by $D_n^{O_2}$ and D_n^{NO} and are not listed in the table below.

C. Chemical reactions: Indirect influence on continuum breakdown

Table II and Fig. 3(a) reveal that in the near wall region along the stagnation line, continuum breakdown is initiated by the diffusion breakdown parameter $D_n^{O_2}$. This section elucidates the competition between the physical mechanisms that drive the system towards nonequilibrium, as well as mechanisms that work to restore the system back to equilibrium.

Consider, for example, the temperature and mole fractions of O and O_2 along the stagnation line leading up to the sphere surface. Compared to the hot gas (~7000 K) in the postshock layer, the relatively cool wall temperature of 2200 K is expected to decrease the gas-phase dissociation of O_2, partially contributing to the observed decrease in the mole fraction of O and the increase in the mole fraction of O_2 near the wall (Fig. 5). Further, the advection and diffusion processes, coupled with wall catalycity effects, result in a high rate of surface recombination. These recombination reactions form O_2, leading to a strong flux of O_2 away from the wall, with the wall acting as a source. Thus, advection and diffusion of O towards the wall produces O_2 through gas-surface recombinations, which in turn leads to diffusion of O_2 away from the wall. The final, steady-state composition of the

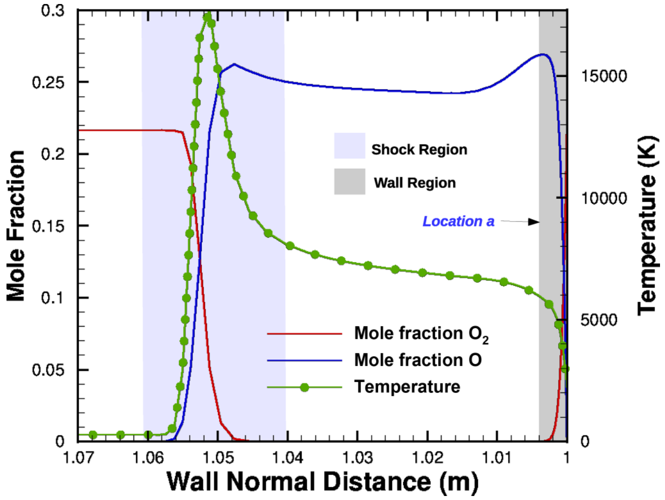

FIG. 5. Variation in temperature and mole fraction of O_2 and O in the flow field along the stagnation line.

gas near the wall depends of the relative balance between the competing physical mechanisms in this region, namely, advection, diffusion, and gas-phase and gas-surface recombination reactions. With this view, the first and second Damköhler numbers $\mathrm{Da_I}$ and $\mathrm{Da_{II}}$, respectively, have been evaluated as [25]

$$\mathrm{Da_I} = \frac{\tau_{\text{advection}}}{\tau_{\text{react}}}, \tag{58}$$

$$\mathrm{Da_{II}} = \frac{\tau_{\text{diffusion}}}{\tau_{\text{react}}} \tag{59}$$

at two locations along the stagnation line: (i) at the start of the near wall breakdown region [~4 mm upstream of the sphere surface (Fig. 5)], henceforth referred to as location a, and (ii) at the sphere surface. Thus, $\mathrm{Da_I}$ compares the advection and reaction time scales, whereas $\mathrm{Da_{II}}$ relates the diffusion and reaction time scales. The ratio of $\mathrm{Da_I}$ to $\mathrm{Da_{II}}$ therefore serves as an indicator of whether the advection or diffusion process dominates in a chosen region of the flow field.

Using the general definition of Damköhler numbers as per Eqs. (58) and (59), three sets of Damköhler numbers $\mathrm{Da_I}$ and $\mathrm{Da_{II}}$ (six Damköhler numbers in all) have been evaluated. The first set compares the time scales of (i) advection with gas-phase reactions at location a ($\mathrm{Da_{I,gas}}$) and (ii) diffusion with gas-phase reaction at location a ($\mathrm{Da_{II,gas}}$). The second set compares the time scales of (i) advection with surface reactions at the sphere wall ($\mathrm{Da}_{\mathrm{I,surf}\,w}$) and (ii) diffusion with surface reactions at the sphere wall ($\mathrm{Da}_{\mathrm{II,surf}\,w}$). The third set compares the time scales of (i) advection with effective surface reactions at location a ($\mathrm{Da}_{\mathrm{I,surf}\,a}$) and (ii) diffusion with effective surface reactions at location a ($\mathrm{Da}_{\mathrm{II,surf}\,a}$).

The first set of Damköhler numbers which is used to assess the relative strength of the diffusion and advection process with respect to gas-phase recombinations, is evaluated at location a as

$$\mathrm{Da_{I,gas}} = \frac{\dot{w}_s l_d}{\rho_s |V|}, \tag{60}$$

$$\mathrm{Da_{II,gas}} = \frac{\dot{w}_s l_d^2}{\rho_s D_s}, \tag{61}$$

where $\dot{w}_s$ is the species production due to gas-phase dissociation and recombination and ρ_s denotes species density. The quantity l_d is the characteristic diffusion length and is taken to be the distance from the sphere wall to location a (~4 mm) for computing all six Damköhler numbers. The

TABLE III. Time scale comparison between diffusion, advection, the gas phase, and surface chemistry.

Position	Reaction considered	Da_{I}	$\mathrm{Da}_{\mathrm{II}}$
location a [Eqs. (60) and (61)]	gas phase	0.000181	0.000270
sphere wall [Eqs. (62) and (63)]	surface	∞	166.3599
location a [Eqs. (65) and (66)]	effective surface	0.1354	0.2021

quantities $|V|$ and D_s denote the velocity magnitude and the diffusion coefficient of the species under consideration at location a. For all the quantities computed in this analysis, atomic oxygen O is the species of interest. The values of $\mathrm{Da}_{\mathrm{I,gas}}$ and $\mathrm{Da}_{\mathrm{II,gas}}$, computed at location a, as per Eqs. (60) and (61) are presented in the first row of Table III.

The second set of Damköhler numbers is evaluated at the sphere wall and provides an assessment of the relative strengths of advection and diffusion of O with respect to surface recombinations of O. These numbers are formulated as

$$\mathrm{Da}_{\mathrm{I,surf}\ w} = \frac{1}{|V|}\gamma_w\sqrt{\frac{k_B T_w}{2\pi m_s}}, \tag{62}$$

$$\mathrm{Da}_{\mathrm{II,surf}\ w} = \frac{l_d}{D_s}\gamma_w\sqrt{\frac{k_B T_w}{2\pi m_s}}, \tag{63}$$

where T_w and m_s are the wall temperature and the particle weight of the atomic species [26]. γ_w is the surface catalycity, and for the fully catalytic wall considered in this work $\gamma_w = 1$. It should be noted that both $|V|$ and D_s are values of velocity magnitude and specieswise diffusion coefficient, respectively, at the sphere wall. The values of $\mathrm{Da}_{\mathrm{I,surf}\ w}$ and $\mathrm{Da}_{\mathrm{II,surf}\ w}$, computed at the sphere wall, as per Eqs. (62) and (63) are presented in the second row of Table III.

The third set of Damköhler numbers is evaluated again at location a and provides an assessment of the relative strength of advection and diffusion of O with respect to effective surface recombinations of O. To translate the influence of surface reactions occurring at the sphere wall to location a, Thoemel *et al.* [26] suggested the use of an effective wall catalycity $\gamma_{\mathrm{effective}}$ given by

$$\gamma_{\mathrm{effective}} = \frac{\text{net recombination of O at location } a}{\text{total incident O at location } a}. \tag{64}$$

Based on this effective wall catalycity, $\mathrm{Da}_{\mathrm{I,surf}\ a}$ and $\mathrm{Da}_{\mathrm{II,surf}\ a}$ can be expressed as

$$\mathrm{Da}_{\mathrm{I,surf}\ a} = \frac{1}{|V|}\gamma_{\mathrm{effective}}\sqrt{\frac{k_B T_a}{2\pi m_s}}, \tag{65}$$

$$\mathrm{Da}_{\mathrm{II,surf}\ a} = \frac{l_d}{D_s}\gamma_{\mathrm{effective}}\sqrt{\frac{k_B T_a}{2\pi m_s}}, \tag{66}$$

where T_a, $|V|$, and D_s are values of gas temperature, velocity magnitude, and specieswise diffusion coefficient, respectively, at location a. The values of $\mathrm{Da}_{\mathrm{I,surf}\ a}$ and $\mathrm{Da}_{\mathrm{II,surf}\ a}$, computed using Eqs. (65) and (66), are presented in the third row of Table III. Thus, a time scale comparison for each of the competing mechanisms that can influence continuum breakdown in the vicinity of the sphere wall, namely, advection, diffusion, gas-phase reactions, and surface recombinations, has been summarized in the form of Damköhler numbers, based on Eqs. (60)–(66), in Table III.

It can be seen from the first row of Table III that the values of Da_{I} and $\mathrm{Da}_{\mathrm{II}}$ at location a are very low. This indicates that gas-phase reactions at the location of breakdown occur on larger time scales compared to that of advection and diffusion.

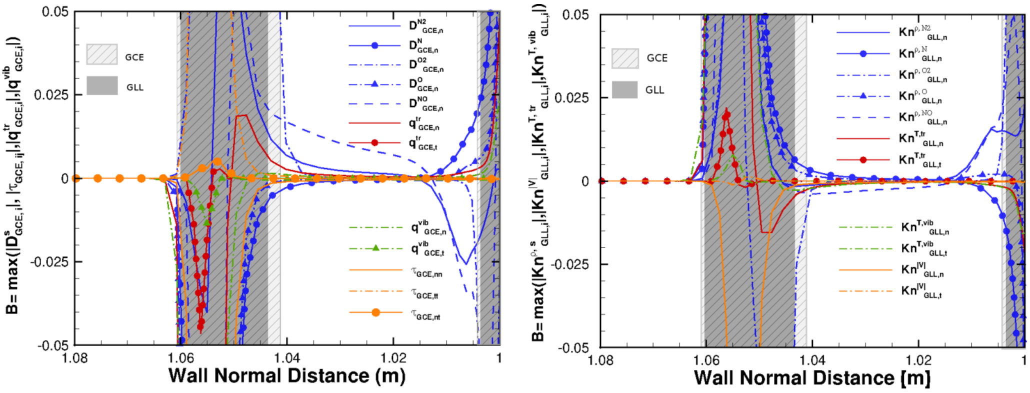

(a) (b)

FIG. 6. Comparison of (a) GCE and (b) GLL breakdown parameters along stagnation line $\theta = 0^\circ$. The hatched areas represent the breakdown region indicated by the GCE parameters, whereas the solid gray fill indicates the breakdown region predicted by the GLL formulation.

The second row of Table III compares the advection and diffusion processes at the wall with the surface recombination rate. At the wall, advection vanishes due to the no-slip velocity boundary condition and the value of Da_{I}, which is a ratio of the advection time scale to the surface reaction time scale, tends to ∞. However, the value of $\mathrm{Da}_{\mathrm{II}}$, the ratio of the diffusion time scale to the surface reaction time scales at the wall, is $O(2)$, indicating that diffusion is mainly responsible for the transport of O towards the wall for initiating surface recombinations. Thus, the molecular flux emerging from the wall is dependent on the rate at which diffusion transports atomic species towards the sphere surface. This diffusion–surface chemistry coupling is responsible for the steep decrease in atomic O that is observed close to the sphere wall (Fig. 5).

The Da_{I} and $\mathrm{Da}_{\mathrm{II}}$ values in the third row of Table III indicate that at location a, both advection and diffusion processes occur on time scales comparable to those of the effective surface recombinations. Thus, the near wall region is characterized by chemical nonequilibrium and the GCE diffusion flux breakdown parameter captures the continuum breakdown resulting from these competing mechanisms.

The GCE diffusion breakdown parameter represents a ratio of the diffusion velocity to the most probable speed of the gas. For the case under study, diffusion and thermal motion of the gas occur on comparable speeds and hence the diffusion breakdown parameter exceeds the breakdown threshold of 0.05 [Fig. 3(a)]. Thus, chemical reactions set up steep concentration gradients giving rise to diffusion fluxes, which in this case are strong enough to distort the equilibrium Maxwellian of the VDF leading to continuum breakdown.

The above analysis indicates that the Damköhler numbers, by comparing the flow and diffusion time scales with the reaction time scale, provide an estimate of the extent of chemical nonequilibrium in the system. It is found that continuum breakdown, as indicated by the GCE specieswise diffusion breakdown parameter, occurs in the regions of strong chemical nonequilibrium.

D. Comparison with the $\mathrm{Kn}_{\mathrm{GLL}}$ breakdown parameters

Figures 6 and 7 show the GCE and GLL breakdown parameters plotted against wall-normal distance along the two extreme angular positions, namely, $\theta = 0^\circ$ and 90°. The $\mathrm{Kn}_{\mathrm{GLL}}$ has been evaluated for translational and vibrational temperature, velocity magnitude, and individual species density based on Eq. (2). The chemically reacting nature of the flow causes species concentrations to fall to very low values at certain locations in the flow field, leading to mathematical anomalies in the computation of the specieswise $\mathrm{Kn}_{\mathrm{GLL}}$. To overcome this, the Q_{local} in Eq. (2) is set to

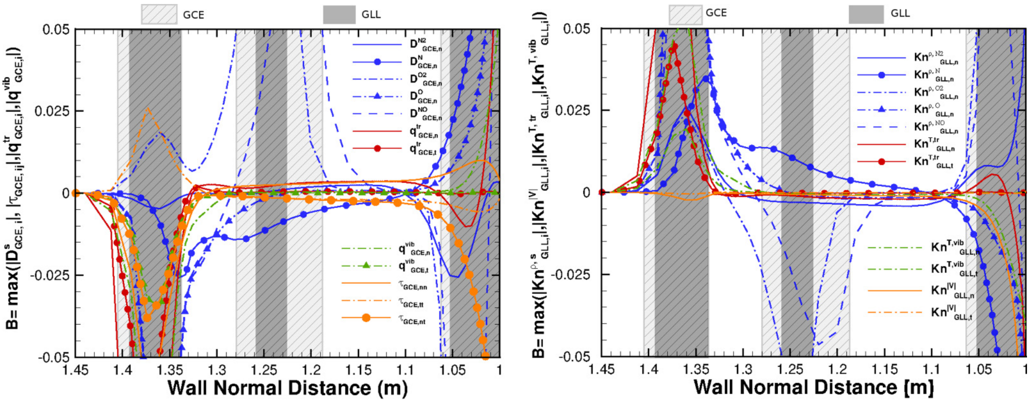

(a)

(b)

FIG. 7. Comparison of (a) GCE and (b) GLL breakdown parameters along $\theta = 90^\circ$. The hatched areas represent the breakdown region indicated by the GCE parameters, whereas the solid gray fill indicates the breakdown region predicted by the GLL formulation.

$\max(\rho_s, 0.001 * \rho_{\text{total}})$, where ρ_{total} is the total density at the location under consideration, similar to procedure employed in the computation of the $D^s_{\text{GCE},i}$.

The GLL breakdown regions are indicated by solid gray fill and the GCE breakdown regions are denoted by the hatched lines, for all continuum breakdown zones. The breakdown regions indicate that at least one of the breakdown parameters has exceeded a threshold value of $B = 0.05$. Thus, these shaded areas represent regions in the flow field where the continuum approximation fails to describe the flow system and a kinetic-based solution methodology needs to be applied.

Figure 6 shows the GCE and GLL breakdown regions, along $\theta = 0^\circ$. Both GCE and GLL breakdown parameters predict the onset of continuum breakdown approaching the shock due to large translational temperature gradients ($q^{\text{tr}}_{\text{GCE},n}$ and $\text{Kn}^{\text{tr}}_{\text{GLL},n}$) at nearly identical locations along the stagnation line $\theta = 0^\circ$ [Figs. 6(a) and 6(b)]. The differences in the prediction of continuum breakdown in approaching the shock becomes apparent for increasing angle θ and is prominent at the $\theta = 90^\circ$ orientation (Fig. 7). It is observed that the GLL formulation predicts the start-of-shock breakdown location slightly downstream of that indicated by the GCE breakdown parameters [Figs. 7(a) and 7(b)]. This shift in the start-of-shock location is likely to arise due to the difference in the coefficients of ∇T in the $q^{\text{tr}}_{\text{GCE},n}$ and $\text{Kn}^{\text{tr}}_{\text{GLL},n}$ parameters. As outlined in Sec. III E, the ratio of $q^{\text{tr}}_{\text{GCE},n}$ to $\text{Kn}^{\text{tr}}_{\text{GLL},n}$ for a single species system is $15\sqrt{\pi}/16$. For the 11-species air mixture considered in this study, this ratio was found to be around 2. As θ increases, the shock strength (and the corresponding temperature gradient) decreases and the disparity between $q^{\text{tr}}_{\text{GCE},n}$ and $\text{Kn}^{\text{tr}}_{\text{GLL},n}$ in predicting the onset of breakdown in the shock region is amplified.

It is observed that $\text{Kn}^{\rho,\text{O}_2}_{\text{GLL},n}$ predicts start of the near wall breakdown region slightly downstream of that indicated by the GCE parameter in Figs. 6 and 7. Similarly, along the $\theta = 90^\circ$ position, the GCE diffusion parameter predicts a larger postshock breakdown region than the corresponding GLL terms. The GCE formulation considers a nondimensionalized form of the specieswise diffusion fluxes to determine continuum breakdown, rather than accounting for only the specieswise density gradients. Further, the representation of diffusion breakdown in the GCE framework considers the contribution of the species number density gradient and pressure gradients to the diffusion driving force, which are responsible for diffusion fluxes [Eq. (18)]. The contribution of this pressure gradient term to the diffusion driving force [Eq. (18)] in turn depends on the abundance and the mass density of the species under consideration, relative to the mixture. Also, the effect of the specieswise diffusion coefficients is also taken into account by the GCE formulation, but the GLL density gradient parameter does not incorporate this feature. These differences in the breakdown parameter definitions are the likely reasons for the disparity in the results observed between the GCE and GLL formulations with regard to specieswise diffusion breakdown.

V. CONCLUSION

The generalized Chapman-Enskog method for rapid and slow processes was used to develop a robust set of continuum breakdown parameters for chemically reacting flows from kinetic theory. These continuum breakdown parameters are derived for one-temperature, two-temperature, and three-temperature models and may readily be applied to analyze continuum breakdown from a CFD flow field solution. The full set of GCE continuum breakdown parameters includes breakdown mechanisms predicted by diffusion processes (multicomponent and thermal), normal and shear stresses, Fourier-type heat fluxes based on translation, rotational, and vibrational temperatures, bulk viscosity, and relaxation pressure. These GCE breakdown parameters, derived from rigorous kinetic theory, are able to accurately capture the proper mechanism leading to the breakdown of all the transport processes, unlike the existing phenomenological breakdown parameters.

The GCE parameters were then used to analyze continuum breakdown for a Mach 24 reacting flow over a sphere. Continuum breakdown was observed due to the strong translational and vibrational heat fluxes at the shock location. Along the stagnation line, the strong species diffusion fluxes due to dissociation and recombination reactions at the shock were also found to perturb the system's VDF. The specieswise diffusion breakdown parameter was instrumental in determining the end-of-shock breakdown location. Diffusion-driven processes resulting from gas-phase and surface chemical reactions were also found to play an important role in determining the location of the near wall breakdown region. Thus, chemical reactions, which are a major source for setting up species concentration gradients, can indirectly distort the VDF by means of strong diffusion fluxes leading to continuum breakdown.

It is also noted that thermal and velocity-slip models have often been employed in CFD calculations to account for noncontinuum effects near a solid surface. While such slip models may be well suited for continuum breakdown in simple gas flows where breakdown due to large velocity gradients (i.e., normal and shear stresses) or temperature gradients (i.e., heat fluxes) dominates, the breakdown occurring due to specieswise diffusion fluxes is not likely to be captured by a slip model.

ACKNOWLEDGMENTS

This work was supported by an Early Career Faculty grant from NASA's Space Technology Research Grants Program (Grant No. NNX15AW46G). The authors gratefully acknowledge Dr. Peter Gnoffo and Dr. Alireza Mazaheri of NASA Langley Research Center for providing the LAURA solutions presented in the analysis.

K.S.-G. and S.S. have contributed equally to this work.

---

[1] G. A. Bird, *The DSMC Method* (Oxford University Press, Oxford, UK, 2013).

[2] R. Roveda, D. B. Goldstein, and P. L. Varghese, Hybrid Euler/particle approach for continuum/rarefied flows, J. Spacecraft Rockets **35**, 258 (1998).

[3] J. M. Burt and I. D. Boyd, A hybrid particle approach for continuum and rarefied flow simulation, J. Comput. Phys. **228**, 460 (2009).

[4] T. E. Schwartzentruber and I. D. Boyd, A hybrid particle-continuum method applied to shock waves, J. Comput. Phys. **215**, 402 (2006).

[5] T. E. Schwartzentruber, L. C. Scalabrin, and I. D. Boyd, A modular particle-continuum numerical method for hypersonic non-equilibrium gas flows, J. Comput. Phys. **225**, 1159 (2007).

[6] V. I. Kolobov, R. R. Arslanbekov, V. V. Aristov, A. A. Frolova, and S. A. Zabelok, Unified solver for rarefied and continuum flows with adaptive mesh and algorithm refinement, J. Comput. Phys. **223**, 589 (2007).

[7] S. Chapman and T. G. Cowling, *The Mathematical Theory of Non-uniform Gases* (Cambridge University Press, Cambridge, 1970).

[8] G. A. Bird, Breakdown of translational and rotational equilibrium in gaseous expansions, AIAA J. **8**, 1998 (1998).

[9] I. D. Boyd, G. Chen, and G. V. Candler, Predicting failure of the continuum fluid equations in transitional hypersonic flows, Phys. Fluids **7**, 210 (1995).

[10] S. Chigullapalli, A. Venkattramana, M. S. Ivanov, and A. A. Alexeenko, Entropy considerations in numerical simulations of non-equilibrium rarefied flows, J. Comput. Phys. **229**, 2139 (2010).

[11] T. R. Deschenes, T. D. Holman, and I. D. Boyd, Effects of rotational energy relaxation in a modular particle-continuum method, J. Thermophys. Heat Transfer **25**, 218 (2011).

[12] T. R. Deschenes and I. Boyd, Extension of a modular particle-continuum method to vibrationally excited, Hypersonic flows, AIAA J. **49**, 1951 (2011).

[13] A. Garcia and B. Alder, Generation of the Chapman-Enskog distribution, J. Comput. Phys. **140**, 66 (1998).

[14] G. A. Bird, *Molecular Gas Dynamics and the Direct Simulation of Gas Flows* (Clarendon, Oxford, 1994).

[15] W. L. Wang and I. D. Boyd, Predicting continuum breakdown in hypersonic viscous flows, Phys. Fluids **15**, 91 (2003).

[16] T. E. Schwartzentruber, L. C. Scalabrin, and I. D. Boyd, Hybrid particle continuum simulations of nonequilibrium hypersonic blunt-body flowfields, J. Thermophys. Heat Transfer **22**, 29 (2008).

[17] J. H. Ferziger and H. G. Kaper, *Mathematical Theory of Transport Processes in Gases* (North-Holland, Amsterdam, 1972).

[18] E. Nagnibeda and E. Kustova, *Non-equilibrium Reacting Gas Flows: Kinetic Theory of Transport and Relaxation Processes* (Springer Science & Business Media, New York, 2009).

[19] K. A. Stephani, D. B. Goldstein, and P. L. Varghese, A non-equilibrium surface reservoir approach for hybrid DSMC/Navier-Stokes particle generation, J. Comput. Phys. **232**, 468 (2013).

[20] P. Gnoffo, Application of program LAURA to three-dimensional AOTV flowfields, *24th Aerospace Sciences Meeting, Reno, Nevada* (AIAA, Reston, VA, 1986).

[21] P. A. Gnoffo, R. S. McCandless, and H. C. Yee, Enhancements to Program LAURA for computation of three-dimensional hypersonic flow, *25th AIAA Aerospace Sciences Meeting, Reno, Nevada* (AIAA, Reston, VA, 1987).

[22] J. D. Ramshaw, Self-consistent effective binary diffusion in multicomponent gas mixtures, J. Non-Equilib. Thermodyn. **15**, 295 (1990).

[23] J. D. Ramshaw and C. H. Chang, Multicomponent diffusion in two-temperature magnetohydrodynamics, Phys. Rev. E **53**, 6382 (1996).

[24] R. N. Gupta, R. A. Yos, J. M. Thompson, and K.-P. Lee, *A review of reaction rates and thermodynamic and transport properties for the 11-species air model for chemical and thermal nonequilibrium calculations to 30000 K*, NASA Report No. NASA-RP-1232, 1990.

[25] R. Brun, *Introduction to Reactive Gas Dynamics* (Oxford University Press, Oxford, 2009).

[26] J. Thoemel, O. Chazot, and P. Barbante, *Proceedings of the 2008 CTR Summer Program* (Stanford University, Stanford, 2008), p. 29.